



**HAL**  
open science

## Magmatic evolution of the Boku Volcanic Complex, Main Ethiopian Rift

Amdemichael Tadesse, Dereje Ayalew, Raphaël Pik, Gezahegn Yirgu, Karen  
Fontijn

► **To cite this version:**

Amdemichael Tadesse, Dereje Ayalew, Raphaël Pik, Gezahegn Yirgu, Karen Fontijn. Magmatic evolution of the Boku Volcanic Complex, Main Ethiopian Rift. *Journal of African Earth Sciences*, 2019, 149, pp.109-130. 10.1016/j.jafrearsci.2018.08.003 . hal-02394249

**HAL Id: hal-02394249**

**<https://hal.univ-lorraine.fr/hal-02394249>**

Submitted on 27 Feb 2024

**HAL** is a multi-disciplinary open access archive for the deposit and dissemination of scientific research documents, whether they are published or not. The documents may come from teaching and research institutions in France or abroad, or from public or private research centers.

L'archive ouverte pluridisciplinaire **HAL**, est destinée au dépôt et à la diffusion de documents scientifiques de niveau recherche, publiés ou non, émanant des établissements d'enseignement et de recherche français ou étrangers, des laboratoires publics ou privés.

# Accepted Manuscript

Magmatic evolution of the Boku Volcanic Complex, Main Ethiopian Rift

Amdemichael Z. Tadesse, Dereje Ayalew, Raphael Pik, Gezahegn Yirgu, Karen Fontijn



PII: S1464-343X(18)30245-0

DOI: [10.1016/j.jafrearsci.2018.08.003](https://doi.org/10.1016/j.jafrearsci.2018.08.003)

Reference: AES 3292

To appear in: *Journal of African Earth Sciences*

Received Date: 7 June 2017

Revised Date: 30 July 2018

Accepted Date: 3 August 2018

Please cite this article as: Tadesse, A.Z., Ayalew, D., Pik, R., Yirgu, G., Fontijn, K., Magmatic evolution of the Boku Volcanic Complex, Main Ethiopian Rift, *Journal of African Earth Sciences* (2018), doi: 10.1016/j.jafrearsci.2018.08.003.

This is a PDF file of an unedited manuscript that has been accepted for publication. As a service to our customers we are providing this early version of the manuscript. The manuscript will undergo copyediting, typesetting, and review of the resulting proof before it is published in its final form. Please note that during the production process errors may be discovered which could affect the content, and all legal disclaimers that apply to the journal pertain.

MAGMATIC EVOLUTION OF THE BOKU VOLCANIC COMPLEX, MAIN ETHIOPIAN RIFT

*Amdemichael Z. Tadesse<sup>1\*</sup>, Dereje Ayalew<sup>1</sup>, Raphael Pik<sup>2</sup>, Gezahegn Yirgu<sup>1</sup> and Karen Fontijn<sup>3</sup>*

*1. School of Earth Sciences, Addis Ababa University, P.O. Box 1176, Addis Ababa, Ethiopia*

*2. CRPG-CNRS, B.P. 20, 54501 Vandoeuvre-le`s-Nancy Cedex, France*

*3. Department of Earth Sciences, University of Oxford, South Parks Road, Oxford OX13AN, United Kingdom*

---

**Corresponding author (\*):** [amdemichael.zafu@aau.edu.et](mailto:amdemichael.zafu@aau.edu.et)

1 MAGMATIC EVOLUTION OF THE BOKU VOLCANIC COMPLEX, MAIN ETHIOPIAN  
2 RIFT

3 *Amdemichael Z. Tadesse<sup>1\*</sup>, Dereje Ayalew<sup>1</sup>, Raphael Pik<sup>2</sup>, Gezahegn Yirgu<sup>1</sup> and Karen*  
4 *Fontijn<sup>3</sup>*

5 1. *School of Earth Sciences, Addis Ababa University, P.O. Box 1176, Addis Ababa,*  
6 *Ethiopia*

7 2. *CRPG-CNRS, B.P. 20, 54501 Vandoeuvre-le`s-Nancy Cedex, France*

8 3. *Department of Earth Sciences, University of Oxford, South Parks Road, Oxford*  
9 *OX13AN, United Kingdom*

---

**Corresponding author (\*):** amdemichael.zafu@aau.edu.et

10

11 **Abstract**

12

13 The Boku volcanic complex is a Quaternary center situated on the axial segment of the Main  
14 Ethiopian Rift (MER), located 92 km South-east from Addis Ababa. The main objective of  
15 this study is to understand the magmatic evolution of the volcanic complex and to develop a  
16 model to answer some outstanding questions related to bimodal products of rift related  
17 volcanism, using geological mapping, petrographic and geochemical approaches. The Boku  
18 complex is characterized by two main phases of activity: pre-caldera/caldera forming  
19 eruptive activity and post-caldera eruptive activity. The volcanic stratigraphy consists from  
20 bottom to top of a sequence of rhyolitic lava flows, pumice flows, welded ignimbrite, pumice  
21 fall, rhyolitic lava dome, obsidian flow, lower basaltic lava flow, ash flow, basaltic scoria and  
22 upper basaltic lava flows. The lithologic varieties together with the geochemical results  
23 indicate that the Boku eruptive products are bimodal in composition; no intermediate  
24 compositions are found. The mafic rocks are transitional to weakly subalkaline basalts while  
25 the silicic rocks are predominantly peralkaline rhyolites. These two groups of rocks are co-  
26 genetic and related to each other by fractional crystallization processes starting from mantle-  
27 derived basaltic magma with a small component of crustal contamination. The available  
28 geophysical, geochemical and field data suggest that the evolution of the evolved silicic  
29 center which hosts a bimodal rock distribution can be explained as a result of prolonged  
30 stagnation of transitional basaltic melt (sourced from the mantle) at relatively high pressures,  
31 where these evolve to intermediate compositions. The transitional basaltic melts can  
32 occasionally erupt to the surface along weakness lines such as faults that infrequently cut the

33 lower part of the shallow reservoir, generating basalts from the intra-caldera and lateral  
34 eruptive centers. We consider the intermediate magma is mechanically trapped at mid-crustal  
35 depths because of its higher crystal load (ca. 50%). Silicic magma is formed at shallow depth  
36 by prolonged fractional crystallization of the intermediate magma and minor assimilation of  
37 crustal material. These silicic magmas generate both effusive and explosive eruption products  
38 in the overall stratigraphy of the volcanic complex.

39

40 Keywords: Boku volcanic complex, Main Ethiopian Rift, eruptive history, petrogenesis,  
41 fractional crystallization, Peralkaline rhyolite, Daly gap.

42

### 43 **1. Introduction**

44 Continental rift zones are sites of lithospheric stretching, which occurs in response to far-field  
45 plate forces such as slab pull, ridge push and tractions at the lithosphere-asthenosphere  
46 boundary induced by mantle flow as a result of sinking oceanic plate (Ring, 2014). The  
47 extension of the crust is achieved through normal faulting that thins the brittle crust; dense  
48 lithospheric mantle rocks rise upward to replace the thinning crust (Buck, 1991; Buck, 2006;  
49 Weissel and Karner, 1989; Bastow et al., 2010; Ebinger and Casey, 2001; Casey et al., 2006).  
50 The East African Rift System (EARS) can be taken as the model example of a continental rift  
51 (Ring, 2014). The EARS is split into Eastern and Western branches. The Eastern branch  
52 extends continuously from the Afar of Ethiopia, through central Ethiopia and Kenya to  
53 northern Tanzania, and is characterized by an almost continuous chain of volcanoes. The  
54 Western branch comprises a series of deep rift basins and distinct volcanic zones, engulfing  
55 the Tanzanian craton on its western side, from Lake Albert in Uganda/DRC down to Lake  
56 Tanganika and further south to the Malawi Rift (Macgregor, 2015; Morley, 1999).

57

58 Previous works (e.g. Ebinger et al., 2000) suggest that the Main Ethiopian Rift (MER)  
59 represents the link region between the Afar triple junction and the Turkana rift in Kenya. The  
60 MER is divided into three main segments; Northern, Central and Southern MER (Corti, 2009;  
61 Mohr, 1983b; Woldegabriel et al., 1990; Hayward and Ebinger, 1996). These segments  
62 reflect different stages of the continental extension process that are interpreted from  
63 differences in fault architecture, timing of volcanism and deformation, and crustal and  
64 lithospheric structure (e.g. Hayward and Ebinger, 1996). The axis of the MER is  
65 characterized by the presence of Quaternary central volcanic complexes which include Boku,  
66 an inconspicuous and very poorly known caldera with numerous scoria cones. The Boku

67 Volcanic Complex (BVC) is located in a transitional zone between the Central and Northern  
68 MER segments at about 92 km from Addis Ababa and 2 km southeast of Adama (Nazret).

69  
70 The MER is a fairly extensively studied segment of the EARS. However, many scientific  
71 questions remain unsatisfactorily solved, particularly those related to the tectono-magmatic  
72 evolution and activity of individual volcanic centers. For instance, after widespread Miocene-  
73 Pliocene volcanism, the Quaternary magmatic activity became mostly localized on the rift  
74 axis, with products showing a typical bimodal composition (dominantly basaltic and rhyolitic  
75 composition). This compositional gap (also known as the Daly gap) remains a poorly  
76 understood aspect of the rift-related magmatism, and different petrogenetic models have been  
77 proposed. Most authors suggest the peralkaline rhyolites to be derived from their parent  
78 basalts by extreme fractional crystallization, whereas others also invoke a component of  
79 crustal contamination (e.g. Gasparon et al., 1993; Peccerillo et al., 2003; 2007; Rooney et al.,  
80 2007; Trua et al., 1999). In addition to this, there is no full agreement among scholars on the  
81 origin of silicic rocks and their relations to mafic rocks (Peccerillo et al., 2007). This study is  
82 motivated by the controversy related to the genesis and relationship between the two groups  
83 of rocks. Large caldera-forming volcanic complexes in the MER such as Gedemsa, Aluto,  
84 Kone and Fanta'Ale have been studied for their eruptive histories and geochemical  
85 characteristics (e.g. Ayalew et al., 2016; Fontijn et al., 2018; Giordano et al., 2014; Hutchison  
86 et al., 2016; 2018; Rampey et al., 2010), but others, like Boku, have not been studied in any  
87 detail. The main objective of our study is, therefore, to describe its eruptive products and  
88 geochemical characteristics for the first time, as well as to better understand the magmatic  
89 evolution. A further objective is to develop a model answer for the question of bimodal  
90 volcanism in a continental rift setting.

91

## 92 **2. Regional Setting**

### 93 **2.1. MER volcanism**

94 The Main Ethiopian Rift (MER) is a key area of the EARS that connects the Red Sea-Gulf of  
95 Aden junction (Afar depression) with the Kenya Rift (Turkana depression) (e.g. Corti, 2009;  
96 Woldegabriel et al., 1990; Hayward and Ebinger, 1996; Mohr, 1983b; Chorowicz, 2005). The  
97 Ethiopian Rift extends for about 1000 km in a NE–SW to N–S direction from the Afar  
98 depression southwards to the Turkana depression. It is ~80 km-wide on average and separates  
99 the uplifted Ethiopian western and eastern plateaus (Mohr, 1983b). MER extensional  
100 deformation started to develop in the late Oligocene-early Miocene (e.g. Ebinger et al., 2000;

101 Bonini et al., 2005; Wolfenden et al., 2004). GPS kinematic data constrains present-day  
102 extension rates to ca. 5 mm/yr (Saria et al., 2014). The adjacent plateaus are mainly made up  
103 of Eocene–Late Oligocene igneous rocks related to the Ethiopian-Yemen flood-basalt  
104 province (Trap series; Corti, 2009; Rooney, 2017). They are predominantly composed of  
105 basalt and intercalated silicic volcanics which have built a sub-aerial volcanic pile, typically  
106 500–1500 m thick and locally attaining 3000 m (Mohr and Zanettin, 1988; Rooney, 2010;  
107 Rooney et al., 2014). The total area presently covered by these volcanic rocks has been  
108 estimated to 600,000 km<sup>2</sup> (Mohr, 1983a). Immediately after the flood basalt eruptive episode  
109 a number of large shield volcanoes developed on the surface of the volcanic plateau from 30  
110 Ma to about 10 Ma (Kieffer et al., 2004; Furman et al., 2006; Rooney et al., 2011).

111  
112 Magmatic activity in the MER has been episodic rather than continuous (Woldegabriel et al.,  
113 1990). After the prevalent Mio-Pliocene volcanism, the Quaternary magmatic activity has  
114 been mostly restricted to the rift floor and is partly associated with a NNE-SSW trending *en*  
115 *echelon* fault system (the Wonji Fault Belt). The Quaternary stages of the rift-related  
116 volcanism have been marked by eruptions of large amounts of silicic rocks from central  
117 volcanoes, basalts predominantly erupted from fissures and scarce intermediate compositions  
118 (e.g. Mohr, 1971; Mohr and Zanettin, 1988; Peccerillo et al., 2003; 2007; Fontijn et al.,  
119 2018). Such a bimodal distribution of chemical compositions is a common feature of many  
120 rift volcanoes, though its origin is still debated (e.g. Rapprich et al., 2016; Giordano et al.,  
121 2014; Boccaletti et al., 1995; Chernet and Hart, 1999; Gasparon et al., 1993; Peccerillo et al.,  
122 2003; 2007; Ronga et al., 2010; Rooney 2010; Rooney et al., 2011; Rooney et al., 2014;  
123 Rooney et al., 2007; Hutchison et al., 2016).

## 124 125 **2.2. Geophysical background on the central MER**

126 The thickness of the crust beneath the MER sharply decreases from the plateau to the rift  
127 axis. On the western and eastern plateau the crustal thickness is ca. 38-40 km (Mackenzie et  
128 al., 2005; Dugda et al., 2005; 2007; Keranen et al., 2009; Keir et al., 2006). Along the rift  
129 axis, the crustal thickness varies from 33-35 km in the northern and central MER, to 24-26  
130 km in southern Afar (Dugda et al., 2005; Keir et al., 2006). Few geophysical data are  
131 available for the southern sector of the MER. Receiver function analysis from the Ethiopian  
132 Broadband Seismic Experiment (Dugda et al., 2005; Maguire et al., 2006) suggest a crustal  
133 thickness decrease in the southern MER to values of ~30 km, consistent with gravity  
134 modeling (Mahatsente et al., 1999). The majority of the crustal thickness variation is lodged

135 in the upper crust, whereas the lower crust is considered to have a relatively constant  
136 thickness. The overall lithospheric strength generally decreases drastically from the Kenyan  
137 to the Ethiopian rift as a result of increasing temperature of the lithosphere (Keranen et al.,  
138 2009).

139  
140 Crustal tomography conveys the existence of elongate bodies along the rift axis of ca. 20 km  
141 wide and 50 km long. These anomalous bodies are separated and laterally offset in a right-  
142 stepping *en-echelon* manner (and coincide with the magmatic segments situated on the floor  
143 of the rift) and characterized by a high  $V_p/V_s$  ratio (Daly et al., 2008; Maguire et al., 2006;  
144 Keranen et al., 2004) and relative positive Bouguer anomalies (Mahatsente et al., 1999).  
145 These bodies are interpreted as cooled mafic intrusions and/or partial melts in the crust and  
146 upper mantle (Daly et al., 2008). The presence of melt is further suggested by shear wave  
147 velocities indicating high temperatures (Keranen et al., 2009; Keranen et al., 2004).

148

### 149 **3. Previous work on Boku Volcanic Complex**

150 Limited knowledge exists on the petrology and geochemistry of BVC. The work by  
151 Boccaletti et al. (1999) and a geological map prepared by Damte et al. (1992) are the only  
152 works that give some information on the distribution, stratigraphy, and geochemical  
153 characteristics of BVC rocks. The 1:50,000 scale geological map of the Nazret-Dera area  
154 by Damte et al. (1992) reveals the general lithologic variations, relative timing and  
155 distribution of tectonic structures. Boccaletti et al. (1999) established the volcanic  
156 stratigraphy of the Nazret-Dera area based on the radiometric dating performed by Bigazzi et  
157 al. (1993) and Morton et al. (1979). Accordingly, the Eastern margin unit consists of the  
158 older volcanic rocks in the stratigraphy and that have an age of ca. 1.8 Ma. The Eastern  
159 margin unit is overlain by Quaternary volcanic products which are associated with the  
160 Wonji Fault Belt (Wonji group). Boccaletti et al. (1999) identified seven geological units  
161 within the Wonji group and grouped the entire suite of volcanic products from the Boku  
162 volcano together as the Boku-Tede Unit (Fig. 4).

163

### 164 **4. Materials and Methods**

165 Detailed field investigations of the eruptive products and tectonic structures at the Boku  
166 Volcanic Complex were carried out in October 2015 and resulted in a volcanological sketch  
167 map of the area. Representative samples were collected for further petrographic and  
168 geochemical analysis. Thin sections were prepared at the School of Earth Sciences, Addis



169 Ababa University. Petrographic studies were performed on a large number of selected  
170 samples, covering the variety of lithologies described in the field.

171

172 Thirty representative samples were then selected for further geochemical analysis. Clean,  
173 non-weathered samples were crushed in a tungsten jaw crusher and powdered using an agate  
174 ball mill. Lithic fragments entrained in ignimbrite were manually removed from the crushed  
175 samples before proceeding with the next step.

176

177 The powdered rock samples were analyzed for major and trace element composition using  
178 Inductively Coupled Plasma Optical Emission Spectroscopy (ICP-OES) and ICP-Mass  
179 Spectroscopy (ICP-MS) respectively, at the Centre de Recherche Pétrographique et  
180 Géochimique (CRPG) of the University of Lorraine, France. Further details on the working  
181 procedure of ICP-OES and ICP-MS are given in Fassel and Kniseley (1974) and Montaser  
182 (1998) respectively. The reproducibility for the different trace elements is comparable to that  
183 presented in other papers using the same facilities and analytical protocols (e.g. Pik et al.,  
184 1999).

185

## 186 **5. Results**

### 187 **5.1. Eruptive products and petrographic descriptions**

188 The volcanic geology of the BVC comprises a wide range of volcanic products as illustrated  
189 in Fig 2. The eruptive units are described according to their stratigraphic succession  
190 (presented in the composite stratigraphy; Fig 2c), as deduced from their vertical contact  
191 relationships in the field and information from published data. The composite stratigraphy is  
192 developed from different outcrops which incorporate more than one eruptive unit. The major  
193 eruptive units identified in the area (from the oldest to the youngest) are: a) rhyolitic lava  
194 flow, b) pumice fall and flow, c) welded ignimbrite, d) rhyolitic lava dome, e) obsidian flow,  
195 f) lower basaltic lava flow, g) ash flow and fall, h) upper basaltic lava and basaltic scoria.  
196 Some additional thin eruptive units comprised of pumice and ash falls and flows are not  
197 included in the composite stratigraphy. These thin eruptive units are, however, presented in  
198 the lithological descriptions below.

199

#### 200 ***a) Rhyolitic lava flow (Qrf)***

201 Rhyolitic lava makes up more than half of the relative thickness in the composite stratigraphy  
202 and comprises two of the ten identified major eruptive units. These rhyolitic lavas are

203 generally grey to pink in colour and occur as lava flows and lava domes. The lowermost  
204 rhyolite lava flow in the stratigraphic succession forms a sharp contact with a pumice flow on  
205 top. The rock is porphyritic with 16-18% phenocrysts and 94-92% groundmass. The  
206 phenocryst is predominantly alkali feldspar (8-9%). The groundmass is microcrystalline and  
207 mainly composed of alkali feldspar and quartz. The rhyolite shows flow banding expressed in  
208 some exposures as clear white and dark red laminations, with a maximum dip of 40°. The  
209 phenocrysts are oriented along the banding and the unit has a maximum vertical thickness of  
210 45 m.

211

#### 212 *b) Pumice fall and flow (Qpl and Qpw)*

213 Unconsolidated pyroclastic deposits occur in two varieties: pumice flow and pumice fall.  
214 These deposits comprise the products of one eruptive sequence with well preserved crystal-  
215 rich pumice clasts. The pumice flow deposits are mainly composed of pumice fragments  
216 (with average grain size of 3.5 cm) in a matrix of finer ash and covers a large area relative to  
217 the pumice fall deposit (6.9 km<sup>2</sup> of pumice flow and 4.9 km<sup>2</sup> of fall deposit). The pumice  
218 lapilli are generally rounded. At different exposures, the pumice flow deposit shows  
219 variations in thickness (up to a maximum of 13 m), and poor sorting, with blocks (up to 7 cm  
220 diameter) of lithic fragments. The lithic fragments are mainly obsidian and rhyolite lava (Fig  
221 3a). The pumice flow deposit is directly overlain by different eruptive units in different  
222 places: pumice fall, rhyolite lava dome or welded ignimbrite. At the southern tip of the Boku  
223 ridge (probably representing the remnant of the caldera rim) the pumice flow deposit is  
224 intercalated with ash flow units (Fig 3b).

225

226 Pumice fall is mainly composed of well-sorted, fine to coarse-grained pumice fragments and  
227 is exposed in different parts of the study area. In the field, two different pumice fall layers are  
228 observed. The lower pumice fall deposit underlies the rhyolite lava flow and has a maximum  
229 thickness of 4 m. The Upper pumice fall layer is observed on top of the rhyolite lava dome  
230 and has a maximum thickness of 1 m. This pumice fall deposit in turn is overlain by ash fall  
231 and ash flow deposits (Fig 3c). Both the lower and upper pumice fall deposits are well sorted,  
232 maintain locally uniform thicknesses, and comprise low-density, grey to yellow-altered,  
233 crystal-poor (alkali feldspar) pumice lapilli up to 7 cm in diameter. The upper pumice fall is  
234 generally finer grained than the lower one. The deposits are mainly exposed along road cuts  
235 and rarely on cliff edges.

236

237 **c) Welded ignimbrite (Qpw)**

238 A welded ignimbrite unit directly overlies the widespread pumice flow. The rock is grey in  
239 color and contains black *fiamme* in some exposures as well as lithic rock fragments. These  
240 rock fragments have a grey color and show flow banding, and are interpreted as rhyolite lava.  
241 The grey to white matrix of the ignimbrite is mostly fine-grained and porphyritic with white  
242 visible crystals. Phenocrysts make up ca. 28% of the rock, and predominantly comprise  
243 quartz (17%), alkali feldspar (8%), Fe-Ti oxides (2%) and pyroxenes (1%). The groundmass  
244 is microcrystalline and mainly composed of quartz and alkali feldspar. From the modal  
245 proportion distribution of the phenocrysts we infer the welded ignimbrite to be rhyolitic in  
246 composition.

247

248 **d) Rhyolitic lava dome (Qrd)**

249 The rhyolitic lava dome represents the greatest thickness in the composite stratigraphy. It  
250 occurs as either grey or pink rhyolite and generally has a flat top surface. In the upper part of  
251 the Boku section, rhyolite lava material intercalates with poorly welded ash flow deposits and  
252 fragmented obsidian. The largest lava dome material at this exposure is approximately 90 m  
253 thick. We interpret the rhyolite to have been dome-forming because of its large height  
254 relative to its width, and the appearance of subvertical flow banding. The rock shows a  
255 hyalopilitic texture, which is a special type of trachytic texture in which alkali feldspar  
256 microlites are oriented parallel and concentric around bigger mineral grains. In thin section  
257 the rhyolite shows a porphyritic texture with small volumetric proportions (18% to 23%) of  
258 phenocrysts. The phenocrysts comprise upto 13% alkali feldspar, 4-7% Fe-Ti oxides and 4-  
259 5% quartz. The groundmass is composed of microcrystalline quartz, alkali feldspar and  
260 reddish stains (that might be clay minerals from hydrothermal alteration).

261

262 **e) Obsidian flow (Qrd)**

263 Obsidian lava flows show a more or less uniform character compared with the other  
264 lithologic units found in the area. Two categories are identified based on physical appearance.  
265 The first one is massive obsidian and the second variety is fragmented and very fragile.  
266 Massive obsidian exposed in the upper part of the stratigraphy, is intercalated with dark grey,  
267 aphanitic rhyolite lava. The fragmented obsidian is intercalated with the rhyolite lava dome  
268 and minor ash fall deposits.

269

270 **f) Lower basaltic lava flow (Qbl)**

271 Basaltic lava flows form a gently sloped terrain in the study area and also exposed along fault  
272 scarps forming steep cliffs. Based on stratigraphy and petrological characteristics, the basaltic  
273 lava flow is classified into two units; lower basalt (Qbl) and upper basalt (Qbu, see section  
274 5.1h). The lower basalt is constituted by a basaltic lava flow underlain by a thin black  
275 scoriaceous base. The scoria fragments range in size from lapilli to blocks. The lava flow has  
276 a maximum thickness of 13.5 m and underlies an ash flow deposit. The rock is mostly  
277 aphanitic but in some areas shows a porphyritic texture. In both cases it is common to  
278 observe a dark grey color and polygonal joints on the rock surface. The porphyritic basalt  
279 comprises 29-55% of phenocryst. The phenocryst contains 18-24% plagioclase feldspar, up  
280 to 15% Fe-Ti oxides, up to 14% olivine, 2% clinopyroxene, 1% orthopyroxene and 1% alkali  
281 feldspar. The mineralogical composition of the plagioclase feldspar is labradorite ( $An_{50-70}$ )  
282 with sporadic bytownite ( $An_{70-90}$ ). The groundmass is microcrystalline and mainly composed  
283 of olivine, plagioclase feldspar and Fe-Ti oxides. This rock unit is exposed only in the  
284 southeastern and northwestern part of the volcano.

285

286 **g) Ash flow and fall (Qra)**

287 Pyroclastic ash flow and fall deposits have the largest coverage in the study area and form  
288 gently sloping to flat terrain. These deposits are generally thin and intercalated with other  
289 lithologies. Based on their physical characteristics, they are classified into two types: ash  
290 flow and ash fall. Matrix-supported ash flow deposits are only represented in one position in  
291 the composite stratigraphy (upper ash flow, Qra), but also occur intercalated with the pumice  
292 flow deposits (Qpw; Fig 2c). In this lower sequence the ash flow deposits obtain a maximum  
293 thickness of 0.7 m, as exposed in Boku section. The upper ash flow (Qra), with a maximum  
294 thickness of 12 m, is overlain by the lower basaltic lava flow and thin alluvial sediments in  
295 the western part of the study area. Generally the ash flow deposits have a pale yellow color,  
296 are moderately welded, poorly sorted, contain lithic fragments and show variations in vertical  
297 thickness. The lithic population is mainly composed of basalt, obsidian and rhyolite up to 3  
298 mm size.

299

300 Ash fall deposits are the second type of fine-grained pyroclastic deposits found in the  
301 volcanic complex. They are not presented in the composite stratigraphy because they are  
302 generally thin. They occur intercalated with pumice fall (Qpl) and ash flow (Qra) deposits.  
303 The ash fall deposits are pale yellow to grey, well sorted, partially indurated and have a

304 consistent local thickness, up to a maximum of 1 m (representing a sequence of different  
305 volcanic pulses).

306

#### 307 *h) Upper basaltic lava (Qbu) and Basaltic scoria (Qbs)*

308 The youngest volcanic products found in the Boku volcanic complex are the upper basaltic  
309 lava flows (Qbu) and underlying basaltic scoria (Qbs). These two varieties are easily  
310 identifiable on a topographic map, as they form cone like structures that are typically  
311 characterized by a gentler slope on one side of the cone. The cones themselves are made of  
312 scoria while the gentle slope is typically formed by the associated basaltic lava flow. Most  
313 cones show an elliptical geometry with their longest axis parallel to the regional tectonic NE-  
314 SW direction, suggesting that their eruption is controlled by preexisting structures (e.g.  
315 Mazzarini et al., 2016).

316

317 Scoria fall deposits are mainly exposed in cliffs and quarries where the materials are  
318 excavated as a raw material for cement production and as aggregates for road construction.  
319 Deposits are red or black, have a maximum thickness of 40 m, and show rhythmic bedding  
320 with blocks and bombs up to 12 cm in diameter.

321

322 The basaltic lava flows (Qbu) are up to 2 m thick and are closely associated with the scoria  
323 deposits. The basalts are dark-grey, porphyritic and vesicular, with some vesicles filled with  
324 secondary minerals. In thin section, they show a seriate texture, with a wide range of  
325 phenocryst grain sizes. The phenocryst population is predominantly made up of plagioclase  
326 feldspar (31%), with Fe-Ti oxides (up to 12%), olivine (9-12%), clinopyroxene (1-2%),  
327 orthopyroxene (1%) and alkali feldspar (1%). The plagioclase feldspar comprises andesine  
328 (An<sub>30-50</sub>) and oligoclase (An<sub>10-30</sub>), and shows oscillatory zoning. The groundmass is composed  
329 of microphenocrysts of the same minerals as the phenocryst population (i.e. predominantly  
330 Fe-Ti oxides, plagioclase feldspar, olivine and pyroxenes).

331

## 332 **5.2. Correlation and eruptive history of Boku Volcanic Complex**

333 The composite stratigraphy of the BVC is correlated with the regional stratigraphy  
334 constructed by Boccaletti et al. (1999) on the basis of our field, petrological and geochemical  
335 data (Fig 4). We suggest our rhyolite lava flow, pumice flow, welded ignimbrite, lower  
336 pumice fall, rhyolite lava dome and obsidian flow (units Qrf to Qrd) to correlate with the  
337 Boku-Tede unit of Boccaletti et al. (1999). The Boku-Tede unit was radiometrically dated

338 using K-Ar dating at 0.51-0.83 Ma (Boccaletti et al., 1999; Bigazzi et al., 1993; Morton et al.,  
339 1979). The products under Boku-Tede are ignimbrite flows, pyroclastic falls, and highly  
340 fractured lava domes with associated obsidian layers (Boccaletti et al., 1999). The lower  
341 basalt lava flow (Qbl) is correlated with their Bofa unit (0.44-0.61 Ma) which have the  
342 characteristics of mafic lava flows with fissural origin; the upper ash flow (Qra) is correlated  
343 with the Dera-Sodore unit (Boccaletti et al., 1999). Finally the basaltic scoria and upper  
344 basaltic lava flows are correlated with the 0.16-0.23 Ma Melkasa (or Wonji) unit (Damte et  
345 al., 1992).

346

347 Our composite stratigraphy and correlation with the primary regional units therefore suggest  
348 that, pre-caldera activity and caldera-forming eruption(s) at Boku took place between 0.51  
349 and 0.83 Ma. Early products in the BVC stratigraphic sequence were mostly effusive, with  
350 the emplacement of rhyolite lava flows. This was followed by a phase of highly explosive  
351 activity emplacing widespread pumice fall and flow deposits, as well as welded ignimbrites,  
352 which were possibly associated with the formation of the caldera. The earliest post-caldera or  
353 latest syn-caldera volcanism, as exposed mainly in the caldera walls, was again effusive, in  
354 the form of rhyolite lava domes. The post caldera eruptive activity at Boku resulted in the  
355 emplacement of the lower basaltic lava flows (at 0.44-0.61 Ma), upper ash flow and finally  
356 basaltic scoria and associated lava flows (since 0.23 Ma).

357

### 358 **5.3. Geochemistry**

359 Major and trace element data were obtained on a representative selection of all major  
360 stratigraphic units to understand the magmatic evolution of the BVC; these data are reported  
361 in Table 1. Loss of Ignition (LOI) is generally low (<2.5 wt%) except for some pumice  
362 samples, where we find LOI values up to 9 wt% (Table 1). These samples also show low  
363 Na<sub>2</sub>O values relative to the rhyolite lava samples, and so the high LOI values are attributed to  
364 post-depositional alteration and the mobile element data on these samples are to be treated  
365 with caution (Peccerillo et al., 2003; Fontijn et al., 2013). In addition to the new geochemical  
366 results, published data from previous works (Rapprich et al., 2016; Giordano et al., 2014;  
367 Boccaletti et al., 1995; Chernet and Hart, 1999; Gasparon et al., 1993; Peccerillo et al., 2003;  
368 2007; Ronga et al., 2010; Rooney 2010; Rooney et al., 2011; Rooney et al., 2014; Rooney et  
369 al., 2007; Hutchison et al., 2016) were used for comparison and are shown as grey fields and  
370 point data in the geochemical diagrams (Fig 5-10).

371



372 5.3.1. **Major element geochemistry**

373 The samples show a typical bimodal composition on the Total Alkali-Silica classification  
374 diagram (after Le Bas et al., 1986, see Fig 5). The distribution of the samples mainly falls on  
375 the subalkaline-alkaline divide, with a felsic field with SiO<sub>2</sub> above 68 wt% and a mafic field  
376 with 45 to 50 wt% SiO<sub>2</sub>. The MgO content of the mafic series ranges from 5.79 to 9.02 wt%.  
377 Nearly all felsic samples are rhyolitic in composition, with two samples near the trachyte-  
378 trachydacite field. All the mafic samples are basaltic in composition and fall within the  
379 transitional to subalkaline field (Fig 5). CIPW norm calculations suggests the basaltic  
380 samples to be olivine-normative (14-24%; nepheline <2%) transitional to weakly subalkaline  
381 basalts (Table 1).

382  
383 The plot of agpaite index against SiO<sub>2</sub> (Fig 6a) shows that the silicic volcanic products  
384 classify as peralkaline rhyolites, except for one pumice sample that has an agpaite index  
385 value of 0.81 and falls in the subalkaline field. The peralkaline rhyolites with low LOI values  
386 indeed have acmite (Ac) in their norm, consistent with their high agpaite index (Table 1).

387  
388 The silicic rocks are further classified on the diagram of Al<sub>2</sub>O<sub>3</sub> against FeO<sub>t</sub> after Macdonald  
389 (1974). The peralkaline rhyolites are reclassified into comendite (three samples) and  
390 pantellerite (the rest of samples; Fig 6b). One sample that was classified as subalkaline based  
391 on its agpaite index (Fig 6a) here classifies as comenditic trachyte.

392  
393 The Harker variation plots are shown in Fig 7 for selected major oxides. These follow the  
394 trends seen at other volcanoes in Ethiopia: positive correlations of TiO<sub>2</sub>, Al<sub>2</sub>O<sub>3</sub>, FeO<sub>t</sub>, CaO,  
395 and P<sub>2</sub>O<sub>5</sub> with MgO and negative correlations of Na<sub>2</sub>O, K<sub>2</sub>O and SiO<sub>2</sub> against MgO (except  
396 for the altered pumice samples which have lower values of Na<sub>2</sub>O, Fig 7f). In addition to the  
397 general trend within similar types of rock (i.e basalt and rhyolite composition) a well-defined  
398 variation trend is shown on the selected major element plots against MgO (Fig 7). The  
399 observed variation in the major element for the mafic and felsic rocks consistently shows  
400 their difference in the evolution stage. The mafic rocks generally exhibit high contents of  
401 TiO<sub>2</sub>, Al<sub>2</sub>O<sub>3</sub>, FeO<sub>t</sub>, MgO, CaO, P<sub>2</sub>O<sub>5</sub> and lower content of Na<sub>2</sub>O, K<sub>2</sub>O and SiO<sub>2</sub> than the felsic  
402 rocks.

403

### 404 5.3.2. Trace element geochemistry

405 The BVC rocks display a wide range of trace element concentration. Fig 8 shows the  
406 variations between selected trace elements and SiO<sub>2</sub>. The compatible trace elements, e.g. Cr,  
407 Sc and Sr, show negative correlations. The incompatible trace elements (e.g. Nb, Zn, Rb, Y  
408 and Zr) show strong positive correlations against SiO<sub>2</sub>. Ba displays incompatible behavior in  
409 the mafic samples and compatible behavior in the silicic samples.

410  
411 Zr displays strong incompatible behavior, with concentrations reaching up to the order of  
412 1000 ppm in the most silicic samples. Zr can therefore be used as a differentiation index. The  
413 incompatible trace elements (e.g. Nb) indeed show a positive correlation with Zr and confirm  
414 that the silicic rocks have a similar evolution history. It is particularly noticeable that the gap  
415 between mafic and silicic samples is narrower when trace elements are plotted against Zr than  
416 against SiO<sub>2</sub> (Fig 9). The diagrams (especially Zr against La, U and Rb) strikingly show  
417 dispersion on the felsic samples which misfit the fractionation trend in the magma evolution.  
418 This dispersal in the incompatible elements can be explained by the interaction of the source  
419 magma with crustal material. The enriched value in the ratio of mobile to refractory trace  
420 elements in felsic rocks (eg., Rb/Nb:0.8-2.8; Th/Ta:1.5-3.8 and Ba/Nb:0.3-15) also further  
421 suggest a possible influence of crustal material in the magmatic evolution history of the BVC.

422  
423 Rare Earth Element (REE) variations are plotted for a selection of mafic and silicic volcanic  
424 products (Fig 10a) normalized to chondrite values (after Boynton, 1984). The enrichment of  
425 the Light REE (LREE) in mafic rocks, expressed in terms of (La/Yb)<sub>N</sub>, ranges between 4.9-  
426 6.4. The gentle slope in Heavy REE (HREE) implies the source for the mafic rocks is garnet-  
427 free. The pattern of the REE diagram is parallel for all samples. This indicates their  
428 derivation from a similar source, with systematic accumulation or removal of mineral phases.  
429 The Eu concentration of mafic lavas shows no clear anomaly (Eu/Eu\*~1.1) which likely  
430 represents no accumulation or fractionation of plagioclase feldspar in the initial stage. The  
431 enrichment of LREE ranges expressed in terms of (La/Yb)<sub>N</sub>. The value ranges between 4.1-  
432 8.7 for the silicic rocks. Similar to mafic samples the silicic samples show parallel patterns in  
433 the REE diagram. All silicic samples show a negative Eu anomaly (Eu/Eu\*<1), which is  
434 typically an indication for the fractionation of plagioclase feldspar.

435  
436 The multi-element spider diagram is shown in Fig 10b normalized to primordial mantle  
437 values (McDonough and Sun, 1995). The diagram for the mafic rocks exhibits a bell-shaped



438 pattern. The diagram further shows a positive anomaly of Ba and a negative anomaly of K  
439 relative to the neighboring trace elements like Nb and La. The combination of minor  
440 enrichment in Ba and troughs in Nb and La may indicate crustal contamination of the mafic  
441 lava during the fractionation process. Overall enrichment in the incompatible elements is  
442 consistent with fractionation of different mineral phases, especially plagioclase feldspar. The  
443 spidergram for the silicic volcanic product shows troughs in Ba, Sr and Ti. Conversely, the  
444 mafic volcanic products have a positive spike in Ba and flatter trends in Sr and Ti. The  
445 negative anomalies and flat trend in Ba and Sr respectively for the two groups of rocks are  
446 indicative of the late crystallization of alkali and plagioclase feldspar. The Ti troughs for the  
447 silicic rocks indicate the removal of accessory ilmenite. Both the mafic and silicic samples  
448 generally exhibit less pronounced positive anomalies in Nb, Th, Pb, K and Ce, and negative  
449 anomalies in U.

450

## 451 **6. Discussion**

### 452 **6.1. Crustal contamination**

453 Before discussing the petrogenesis of the Boku peralkaline rhyolitic rocks it is essential to  
454 assess the degree of crustal contamination. From the different diagrams discussed above we  
455 can infer that crustal contamination plays a small role in the compositional evolution of the  
456 magmas.

457

458 Besides the ratio of mobile to refractory trace elements (discussed in section 5.3.2) crustal  
459 material involvement is mainly evaluated using the contamination index (La/Nb) and Nb and  
460 Ta patterns in the spidergram (Hofmann, 2003; Ayalew and Gibson, 2009; Rudnick and Gao,  
461 2003). Some Boku samples show La/Nb ratios above 1, with a maximum value of 1.24 which  
462 may indicate slight contamination by crustal material. The diagrams of La/Nb and Th/Ta  
463 against SiO<sub>2</sub> show a slight sub-horizontal to inclined trend (Fig 11a and b) further suggesting  
464 minor contamination. The high value of Th/Nb (0.1-0.3) further traces the involvement of  
465 crustal material. Crustal contamination has also been suggested in the wider region using  
466 trace element and isotope geochemistry (e.g. Gedemsa, Fanta'Ale, Boset and Aluto;  
467 Giordano et al., 2014; Ronga et al., 2010; Hutchison et al., 2016; 2018). Compared to  
468 Fanta'Ale and Gedemsa (Giordano et al., 2014) the La/Nb and Th/Ta values indicate a slight  
469 increment in the case of BVC (Fig 11a and b). This further substantiates the existence of  
470 crustal contamination in BVC samples and suggests that the degree of contamination is  
471 slightly higher than in the two other volcanoes. Some BVC silicic rocks show low Nb

472 concentrations down to 42 ppm (Table 1). One sample from the mafic rocks shows lower  
473 values of Ce/Pb (10) and Nb/U (30) compared to average MORB and IOB values (Ce/Pb=  
474  $25\pm 5$ ; Nb/U= $47\pm 10$ ; Hofmann et al., 1986) which further suggest a small involvement of  
475 crustal material.

476

## 477 **6.2. Petrogenesis of silicic rocks**

478 Some of the outstanding questions related to peralkaline volcanism relate to the origin of  
479 peralkaline silicic rocks, their relationship with basaltic magmas, and the reasons for the  
480 paucity of intermediate compositions in the eruptive volcanic products. The data presented in  
481 this study reveal, in agreement with previous studies, that the Quaternary volcanism in the  
482 MER is dominated by a bimodal association of mafic and silicic products, with scarce or no  
483 intermediate rocks. This bimodality is also seen at Fanta' Ale and Gedemsa (e.g. Peccerillo et  
484 al., 2003; 2007; Giordano et al., 2014) and only small proportions of intermediate rocks are  
485 observed at Boset-Bericha and Aluto (e.g. Macdonald et al., 2012; Ronga et al., 2010;  
486 Hutchison et al., 2016; 2018; Siegburg et al., 2018).

487

488 The observation that the REE diagram is flatter in the heavy REE region ( $Tb_n/Yb_n=0.34-0.37$   
489 and nearly constant Y and Yb concentration), in combination with low CaO/Al<sub>2</sub>O<sub>3</sub> (0.6-0.8)  
490 and Zr/Y ratios (5-14), suggests that the source of the mafic rocks is garnet-free. The mafic  
491 samples exhibit the following compositional ranges: MgO (5.79-9.77 wt%), Cr (158-581  
492 ppm) and Ni (31-154 ppm); and are therefore more evolved than primary MORB magmas  
493 (after Frey et al., 1978; Baker et al., 1996; Kushiro, 1996; Allègre et al., 1977). From this we  
494 infer that the mafic rocks at BVC have undergone moderate fractionation of olivine and  
495 clinopyroxene (suggested from solidification indices and Mg# <50). The Ba/Nb ratio ranges  
496 10 to 22.8 with an average value of 16.4. This value is higher than the average value for  
497 primitive mantle (after McDonough and Sun, 1995), and this can be attributed to  
498 contamination by continental crust (Ba/Nb=57; Rudnick and Gao, 2003) and/or fractionation  
499 processes.

500

501 The major and trace element compositions are used to evaluate whether the mafic and silicic  
502 rocks are genetically related or not. The Harker diagrams have two clusters of sample  
503 distribution separated by a wide compositional gap commonly referred to as the Daly gap  
504 (e.g. Bunsen, 1851; Daly, 1925; Peccerillo et al., 2003; Macdonald et al., 2008; Ferla and

505 Meli, 2006; Lowenstern et al., 2006). The presence of this compositional gap does however  
506 not preclude the genetic association of the rocks. The gap significantly narrows when highly  
507 incompatible trace elements are considered as a differentiation index. This is illustrated in Fig  
508 9 where selected trace elements are plotted against Zr. These plots show positive correlations  
509 with slopes of approximately 1. Such a relationship is commonly interpreted as indicative of  
510 the genetic relationship or co-genetic nature of the mafic and silicic rocks (e.g. Hutchison et  
511 al., 2016). Apart from using elemental concentrations to determine the source resemblance of  
512 the volcanic suites, the systematic behavior of some highly incompatible element ratios like  
513 Nb/Ta, Zr/Hf and Ce/Pb are strong indicators of the co-genetic nature of the magmas. These  
514 ratios do not change significantly in lavas from the same source. The highly incompatible  
515 element ratios like Nb/Ta (11-14), Zr/Hf (35-42) and Ce/Pb(7-14) show a narrow range  
516 which can determine the genetic relationships of the mafic and felsic suits. This is further  
517 supported in spidergrams and multi-element variation diagrams in which mafic and silicic  
518 rocks of selected samples show parallel patterns, exhibited by a marked LREE enrichment  
519 relative to HREE, like also seen at other volcanoes in the MER (Ayalew and Gibson, 2009;  
520 Ronga et al., 2010; Trua et al., 1999). This result can be substantiated by further analysis of  
521 isotope (especially Sr and Nd isotopes).

522  
523 Several hypotheses have been proposed to explain the genesis of peralkaline volcanism in the  
524 Ethiopian rift (Trua et al., 1999; Peccerillo et al., 2007). The first one is partial melting of the  
525 old continental crust (crustal anatexis) and basalt (e.g. Thy et al., 1990; Hay and Wendlandt,  
526 1995; Beard and Lofgre, 1991). The second mechanism is a two-step of process; partial  
527 melting followed by fractional crystallization (e.g. Trua et al., 1999; Bohrsen and Reid,  
528 1997); the third is fractional crystallization with little involvement of crustal material (e.g.  
529 Peccerillo et al., 2003; Giordano et al., 2014; Hutchison et al., 2016). Crustal anatexis alone  
530 cannot explain the petrogenesis of the peralkaline volcanic products (Peccerillo et al., 2003).  
531 The geochemical composition of Ethiopian Precambrian rocks that constitute the basement is  
532 compared with our data of BVC samples. If crustal anatexis played a significant role, melting  
533 processes (i.e. partial melting) would be expected to drive up the ratios of incompatible  
534 elements (e.g. Rb/Nb and Rb/Zr) in the melt (BVC in this case) relative to the source  
535 (Precambrian rock), which is not the case in our sample set (Table 2). Crustal anatexis is  
536 therefore unlikely to play a significant role in the formation of peralkaline rocks of Boku. The  
537 incompatible element ratios of BVC rocks are also very low when compared to the flood

538 basalts (e.g. Kieffer et al., 2004). This indicates that partial melting of the Ethiopian flood  
539 basalt cannot explain the petrogenesis of Boku volcanic products either.

540

### 541 **6.3. Fractional crystallization**

542 Our major and trace element data are consistent with a fractional crystallization trend that is  
543 dominated by the removal of different mineral phases at different stages of the fractionation.  
544 The sharp, steep positive correlations of  $\text{FeO}_t$  and  $\text{MgO}$  are attributed to the crystallization of  
545 ferromagnesian mineral phases (olivine and pyroxenes). Another phase that fractionates from  
546 the system is plagioclase feldspar, as indicated by the decrease of  $\text{CaO}$ ,  $\text{Al}_2\text{O}_3$  and  $\text{Sr}$ .  
547 Ilmenite and apatite are also interpreted to fractionate from the system based on the decrease  
548 in  $\text{TiO}_2$  and  $\text{P}_2\text{O}_5$ . Finally, late-stage alkali feldspar fractionation is suggested by the negative  
549 correlations of  $\text{K}_2\text{O}$ ,  $\text{Na}_2\text{O}$  and  $\text{Ba}$  in the high- $\text{SiO}_2$  compositions. The dominance of alkali  
550 feldspar fractionation in highly evolved rhyolite is further supported by the field description  
551 and petrographic observations on thin sections. The role of the fractionation process is  
552 significantly visible within the silicic and basaltic groups of rocks (Fig 7). In terms volatile  
553 exsolution from the magma, fractionation plays a significant role in the magmatic history of  
554 BVC. This process increases the explosively of the magma which is clearly visible in the pre  
555 to syn eruptive sequence of BVC.

556

557 Both batch and partial melting processes are able to generate liquids with variable  
558 enrichments in incompatible elements, but with moderate depletion in compatible elements.  
559 In contrast, fractional crystallization is much more efficient in producing compatible element  
560 depletion than incompatible element enrichment (Ayalew et al., 2002; Ayalew and Gibson,  
561 2009; Peccerillo et al., 2003). Therefore, models of incompatible against compatible trace  
562 elements are potentially powerful tools to further discriminate between fractional  
563 crystallization and partial melting processes.  $\text{Sr}$  against  $\text{Rb}$  is plotted for this purpose (Fig  
564 12a). The plot shows strong variations in compatible element concentrations ( $\text{Sr}$ ) and only  
565 limited variations in incompatible element concentrations ( $\text{Rb}$ ), suggesting that fractional  
566 crystallization is the dominant process in the magmatic differentiation of BVC rocks.

567

### 568 **6.4. Petrogenetic modeling**

569 In this section the evolution of BVC silicic magmas is modeled. The parent magma selected  
570 is sample NB-01, one of the least differentiated in our suite of samples ( $\text{MgO}$  8.81 wt%;  $\text{Ni}$   
571 88 ppm). The partition coefficients selected for the model are 4.7 for  $\text{Sr}$  and 0.029 for  $\text{Rb}$

572 (Ewart and Griffin, 1994). A model of fractional crystallization has been tested by following  
 573 Rayleigh's law from the least differentiated basalt sample using the equation (after Neuman  
 574 et al., 1954):

575

576  $C_L^i = C_o^i F^{(D^i-1)}$ ; where  $C_L^i$ : concentration of trace element i in the liquid

577  $C_o^i$ : concentration of trace element i in the parent magma

578 F: weight proportion of liquid

579  $D^i$ : bulk distribution coefficient for element i.

580 By applying the above equation we calculate the degree of fractionation and the  
 581 concentrations of the daughter liquid. To generate the silicic BVC compositions, the mafic  
 582 magma needs at least a degree of fractional crystallization of 80% (Fig 12b). At this degree of  
 583 fractionation the composition of the calculated liquids is very similar to that of the analyzed  
 584 liquid for all trace elements, except for Pb and Sr (Fig 12c and d). The resulting data can be  
 585 explained by the fractionation process occurring in open system and allowing interaction of  
 586 the magma with the surrounding crustal material.

587

588 Rhyolite-MELTS software (after Gualda et al., 2012) is applied to further understand the  
 589 crystallization sequence of the highly evolved magma from their parent basaltic magmas. The  
 590 simulation is applied at different pressure conditions (0.3 kbar to 2 kbar). The process of  
 591 crystallization was checked against various buffer systems and it was found that the QFM  
 592 buffer system produces peralkaline magma. The crystallization series for different pressure  
 593 conditions shows that the silica content increases from low to medium pressure (0.6 kbar) and  
 594 starts to decline at higher pressure. The graphs (Fig 13a) show the typical pressure conditions  
 595 that can be applied to the formation of peralkaline magma; 0.5, 0.6 and 0.7 kbar. The  
 596 fractionation and ponding of magma at shallow crustal level is consistent with results of  
 597 geochemical and geophysical studies of Gedemsa volcano and the MER rift axis volcanic  
 598 centers (e.g. Peccerillo et al., 2003; Rooney et al., 2011; Keranen et al., 2009; Keranen et al.,  
 599 2004). At these shallow pressure conditions the degree of fractionation is very similar to that  
 600 constrained by our trace element modeling (F=88 to 90%). Under pressure conditions which  
 601 can produce peralkaline magma, first the basaltic magmas fractionate to intermediate  
 602 compositions and then progressively produce peralkaline magma (Fig 13b). Our Rhyolite-  
 603 MELTs modeling at low pressure (e.g. 0.6 kbar) indicates that the first phase to crystallize  
 604 and fractionate from the primitive basaltic melt is olivine at  $1141 \pm 30$  °C (Fig 13c). Olivine

605 fractionation is then followed by plagioclase feldspar, clinopyroxene and spinel crystallizing  
606 at a temperature of  $1091\pm 40$  °C in different proportions. Orthopyroxene and apatite follow at  
607  $991\pm 30$  °C and finally Fe-Ti oxides start crystallizing at a temperature of  $941\pm 35$  °C. The  
608 crystallization of different mineral phases ends at  $841\pm 40$  °C.

609  
610 The proportions of fractionating mineral phases are constrained by mass balance calculation  
611 following the methods of Stormer and Nicholls (1978). The chemical composition of each  
612 mineral phase is adopted from Boccaletti et al. (1999) who analyzed samples collected in the  
613 study area. The validity of the model was confirmed by the r-squared ( $r^2$ ) value. The mass  
614 balance modeling is tested in different ways by considering either fractional crystallization or  
615 fractional crystallization with involvement of crustal material. The average upper crust  
616 composition (after Taylor and McLennan, 1985) and the Ethiopian basement rocks  
617 composition (adopted from Alene et al., 2000; Teklay et al., 1998; Asrat and Barbey, 2003)  
618 are considered for the crustal contaminant composition by the optimization technique in the  
619 OPTIMASBA modeling workbook (Cabero et al., 2012). To obtain the least differentiated  
620 rhyolitic material in the Boku sample set (i.e. sample NB-22; Table 1) with no involvement  
621 of crustal material, the primitive basalt fractionates the following minerals: 21% olivine, 14%  
622 clinopyroxene, 56% plagioclase feldspar, 8% Fe-Ti oxides and minor apatite (~1%). The  $\Sigma r^2$   
623 is 0.97 in this case. The best fit regression coefficient becomes even better ( $\Sigma r^2=0.99$ ) when  
624 crustal contamination with 0.1 relative ratio of assimilated to crystallized material is  
625 considered in the modeling. The proportions of the fractionating minerals (26% olivine, 14%  
626 clinopyroxene, 65% plagioclase feldspar, 8% Fe-Ti oxides and minor apatite ~1%.) show a  
627 significant change compared to the first model. The most differentiated peralkaline rhyolite  
628 (i.e. NB-14; Table 1) is further derived from the least differentiated rhyolite by alkali feldspar  
629 and quartz fractionation.

630  
631 Our major and trace element modeling suggests there is formation of intermediate magma  
632 composition. Field observations around Boku volcano and most other MER volcanic centers;  
633 however, shows scarce occurrences of intermediate erupted magmas. Therefore, the rare  
634 occurrences of intermediate magmas may possibly be related to their non-eruption (e.g.  
635 Macdonald 2012; Ronga et al., 2010). Small proportions of intermediate magma formation  
636 have been ascribed to a sudden drop followed by a rapid increase in oxygen fugacity during  
637 the crystallization of Fe-Ti oxides near the transition to peralkalinity (eg. Barberi et al.,



1975). This hypothesis is not verified by our major element modeling. The Boku least evolved trachyte-trachydacite compositions are peralkaline already and the Fe-Ti oxides are started to crystallize only after the intermediate magmas have been formed (at  $941\pm 35$  °C). Physical controls such as density and/or viscosity can inhibit the ascent of magmas with specific compositions (e.g. Baker et al., 1977; Jones 1979). At centers where intermediate magmas are found (e.g. Boset); these tend to contain high proportions of crystals (eg. Peccerillo et al., 2003; Ronga et al., 2010). The non-eruption of similar intermediate magmas at centers like Boku is therefore possibly related to the high effective viscosities resulting from the high crystal load, in combination with higher densities of magmas. Some experimental and modeling studies (e.g. Marsh 1981; Dufek and Bachmann, 2010; Bonnefoi et al., 1995; Brophy 1991) indeed suggest mechanical trapping of melt by a high crystal load. Melts in these models can only be extracted from the mixture composition after critical crystallization (40-50 vol% crystals). This critical crystal fractionation can change the composition of the mixed magma to silicic and facilitate the melt extraction. Silicic rhyolite melt would generate magmas with even higher viscosities, but also a lower density, facilitating their extraction (e.g.  $2400-2600$  kg/m<sup>3</sup> for intermediate and  $<2400$  kg/m<sup>3</sup> for silicic melts; Peccerillo et al., 2003). This density difference and generally higher volatile contents (resulting from fractional crystallization) of the silicic magmas may further help to drive them to the surface.

By taking into account the existing geochemical, geophysical and field observation data we can explain the evolution of silicic centers in the MER which comprise mafic and silicic, but scarce or no intermediate volcanic products (Fig 13d). The transitional basaltic melts sourced from upper mantle stagnate at relatively deep level (Bastow et al., 2010; Daly et al., 2008; Maguire et al., 2006; Keranen et al., 2004; Mahatsente et al., 1999) and evolves to intermediate magma compositions. Sometimes the transitional basaltic melt may erupt directly to the surface along structural weaknesses such as faults that infrequently cut the lower parts of the shallow magma reservoirs, and generate basaltic lava flows and scoria cones from intra-caldera and lateral centers (e.g. Peccerillo et al., 2007; Mazzarini et al., 2016). The mush of the intermediate magma has a higher opportunity for mechanical trapping at intermediate depth because of its high crystal load of ca. 50%. Silicic magma will be formed at shallow depths by prolonged fractional crystallization and minor assimilation of the intermediate magma. The variable amounts of volatiles in the silicic melts sometimes

671 produce explosive eruptions and resulting pyroclastic deposits, alongside obsidian flows and  
672 domes in the stratigraphic sequence.

673

## 674 **7. Conclusions**

675 A combination of field mapping, petrography and geochemistry provides new perceptions  
676 about the eruptive history and magmatic evolution of the Boku volcanic complex and the  
677 adjacent silicic centers in the Main Ethiopian Rift. The main conclusions of this study are:

678 1. The Boku volcanic complex is composed of volcanic products sourced from two main  
679 episodes of volcanic activity: Boku pre-caldera/caldera forming eruptive activity and  
680 post-caldera eruptive activity. The Boku pre-caldera/caldera forming activity was initially  
681 predominantly effusive, then culminated in an explosive phase and finally became non-  
682 explosive again. This eruptive activity took place between 0.51-0.83 Ma. The main  
683 volcanic products are rhyolitic lava flow, pumice flow, welded ignimbrite, pumice fall,  
684 and rhyolitic lava dome and obsidian flow. The post-caldera volcanic activity occurred  
685 between 0.16-0.23 Ma. This activity resulted mainly in ash flows, basaltic scoria and  
686 basaltic lava flows.

687

688 2. The petrographic observations and major element geochemistry reveals that the BVC  
689 rocks are bimodal, i.e. predominantly basaltic and rhyolitic, with no intermediate  
690 compositions found. The basalts are transitional to weakly subalkaline while the silicic  
691 rocks are predominantly peralkaline rhyolite.

692

693 3. The major and trace element geochemistry strongly suggests that the basalts and  
694 peralkaline rhyolites are genetically related. Major and trace element variations and  
695 modeling imply that the rocks are linked by fractional crystallization processes with  
696 minor to no crustal contamination. In order to form Boku peralkaline rocks, the parental  
697 basaltic magma needs to have undergone at least 80% fractional crystallization.

698

699 4. The available geophysical, geochemical and field data suggest that the bimodal rock  
700 distribution of the Boku Volcanic Centre can be explained as a result of prolonged  
701 stagnation of transitional basaltic melt (sourced from the mantle) at relatively high depth,  
702 which evolves to intermediate magma compositions. Occasionally the transitional basaltic  
703 melt erupts to the surface along structural weaknesses, to produce basaltic eruptive  
704 products from intra-caldera and lateral vents. The intermediate magma possibly be



705 trapped mechanically at intermediate depth because of its high crystal load. Silicic  
706 magma can finally be formed at shallow depth by prolonged fractional crystallization and  
707 minor assimilation of the intermediate magma, and produce explosive as well as effusive  
708 eruptions.

709

### 710 **Acknowledgments**

711 This research was part of the first author's MSc. thesis work. Financial support was provided  
712 by a studentship at the School of Earth Science, Addis Ababa University and a research  
713 project grant funded by European Research Council and Deep Carbon Observatory (grant  
714 number 267255). Karen Fontijn is supported by the UK's Natural Environment Research  
715 Council grant NE/L013932/1 (RiftVolc). Different individuals helped by assisting the field  
716 work, thin section sample preparation and providing wealthy information about the subject of  
717 study; they are Mr. Bahru Zinaye, Mr. Samuel Getachew, Mr. Million Alemayehu and Mr.  
718 Wondwossen Sisay. We thank Dr. Mulugeta Alene, Prof. Tanya Furman and one anonymous  
719 reviewer for expert reviews that have greatly improved the paper. Dr. Read Mapeo is highly  
720 acknowledged for editorial handling.

721

722

723

724

725

726

727

728

729

730

731

732

733

734

735

736

737

738 **Reference**

- 739 Alene, M., Ruffini, R., and Sacchi, R. (2000). Geochemistry and geotectonic setting of  
740 Neoproterozoic rocks from northern Ethiopia (Arabian-Nubian Shield). *Gondwana*  
741 *Research*, **3**(3):333-347.
- 742 Allègre, C. J., Treuil, M., Minster, J. F., Minster, B., and Albarède, F. (1977). Systematic use  
743 of trace element in igneous process. *Contributions to Mineralogy and*  
744 *Petrology*, **60**(1):57-75.
- 745 Asrat, A., and Barbey, P. (2003). Petrology, geochronology and Sr–Nd isotopic geochemistry  
746 of the Konso pluton, south-western Ethiopia: implications for transition from  
747 convergence to extension in the Mozambique Belt. *International Journal of Earth*  
748 *Sciences*, **92**(6):873-890.
- 749 Ayalew, D., Barbey, P., Marty, B., Reisberg, L., Yirgu, G., and Pik, R. (2002). Source,  
750 genesis, and timing of giant ignimbrite deposits associated with Ethiopian continental  
751 flood basalts. *Geochimica et Cosmochimica Acta*, **66**(8):1429-1448.
- 752 Ayalew, D., and Gibson, S. A. (2009). Head-to-tail transition of the Afar mantle plume:  
753 Geochemical evidence from a Miocene bimodal basalt–rhyolite succession in the  
754 Ethiopian Large Igneous Province. *Lithos*, **112**(3):461-476.
- 755 Ayalew, D., Jung, S., Romer, R. L., Kersten, F., Pfänder, J. A., and Garbe-Schönberg, D.  
756 (2016). Petrogenesis and origin of modern Ethiopian rift basalts: Constraints from  
757 isotope and trace element geochemistry. *Lithos*, **258**:1-14.
- 758 Baker, B. H., Goles, G. G., Leeman, W. P., and Lindstrom, M. M. (1977). Geochemistry and  
759 petrogenesis of a basalt-benmoreite-trachyte suite from the southern part of the  
760 Gregory Rift, Kenya. *Contributions to Mineralogy and Petrology*, **64**(3):303-332.
- 761 Baker, J., Snee, L., and Menzies, M. (1996). A brief Oligocene period of flood volcanism in  
762 Yemen: implications for the duration and rate of continental flood volcanism at the  
763 Afro-Arabian triple junction. *Earth and Planetary Science Letters*, **138**(1-4):39-55.
- 764 Barberi, F., Ferrara, G., Santacroce, R., Treuil, M., and Varet, J. (1975). A transitional basalt-  
765 pantellerite sequence of fractional crystallization, the Boina Centre (Afar Rift,  
766 Ethiopia). *Journal of Petrology*, **16**(1):22-56.
- 767 Bastow, I. D., Pilidou, S., Kendall, J. M., and Stuart, G. W. (2010). Melt-induced seismic  
768 anisotropy and magma assisted rifting in Ethiopia: Evidence from surface  
769 waves. *Geochemistry, Geophysics, Geosystems*, **11**(6).

- 770 Beard, J. S., and Lofgren, G. E. (1991). Dehydration melting and water-saturated melting of  
771 basaltic and andesitic greenstones and amphibolites at 1, 3, and 6. 9 kb. *Journal of*  
772 *Petrology*, **32**(2):365-401.
- 773 Bigazzi, B., Bonadonna, F., Di Paola, G., and Giuliani, A. (1993). K-Ar and fission track  
774 ages of the last volcano tectonic phase in the Ethiopian Rift Valley (Tullu Moye area).  
775 *Geology and mineral resources of Somalia and surrounding regions. Istituto*  
776 *Agronomico Oltremare, Firenze, Relazioni Monografie*, **113**:311-322.
- 777 Boccaletti, M., Assefa, G., Mazzuoli, R., Tortorici, L., and Trua, T. (1995). Chemical  
778 variations in a bimodal magma system: the Plio-Quaternary volcanism in the Dera  
779 Nazret area (Main Ethiopian Rift, Ethiopia). *Africa Geoscience Review*, **2**(1):37-60.
- 780 Boccaletti, M., Mazzuoli, R., Bonini, M., Trua, T., and Abebe, B. (1999). Plio-Quaternary  
781 volcanotectonic activity in the northern sector of the Main Ethiopian Rift:  
782 relationships with oblique rifting. *Journal of African Earth Sciences*, **29**(4):679-698.
- 783 Bohrsen, W. A., and Reid, M. R. (1997). Genesis of silicic peralkaline volcanic rocks in an  
784 ocean island setting by crustal melting and open-system processes: Socorro Island,  
785 Mexico. *Journal of Petrology*, **38**(9):1137-1166.
- 786 Bonnefoi, C. C., Provost, A., and Albarede, F. (1995). The 'Daly gap' as a magmatic  
787 catastrophe. *Nature*, **378**(6554):270.
- 788 Bonini, M., Corti, G., Innocenti, F., Manetti, P., Mazzarini, F., Abebe T., and Pecskey, Z.  
789 (2005). Evolution of the Main Ethiopian Rift in the frame of Afar and Kenya rifts  
790 propagation. *Tectonics*, **24**(1).
- 791 Boynton, W. (1984). *Cosmochemistry of the rare earth elements*. Elsevier.
- 792 Brophy, J. G. (1991). Composition gaps, critical crystallinity, and fractional crystallization in  
793 orogenic (calc-alkaline) magmatic systems. *Contributions to Mineralogy and*  
794 *Petrology*, **109**(2):173-182.
- 795 Buck, W.R. (1991). Modes of continental lithospheric extension. *Journal of Geophysical*  
796 *Research: Solid Earth*, **96**(B12):20161-20178.
- 797 Buck, W.R., 2006. The role of magma in the development of the Afro-Arabian rift  
798 system. In: Yirgu, G., Ebinger, C., Maguire, P. (Eds.), *The Afar Volcanic Province*  
799 *within the East African Rift System. Special Publication of the Geological Society,*  
800 *London, pp. 43–54.*
- 801 Bunsen, R. (1851). Ueber die Prozesse der vulkanischen Gesteinsbildungen Islands. *Annalen*  
802 *der Physik*, **159**(6):197-272.

- 803 Cabero, M. T., Mecoleta, S., and López-Moro, F. J. (2012). OPTIMASBA: A Microsoft  
804 Excel workbook to optimise the mass-balance modelling applied to magmatic  
805 differentiation processes and subsolidus overprints. *Computers &*  
806 *geosciences*, **42**:206-211.
- 807 Casey, M., Ebinger, C., Keir, D., Gloaguen, R., and Mohamed, F. (2006). Strain  
808 accommodation in transitional rifts: extension by magma intrusion and faulting in  
809 Ethiopian rift magmatic segments. *Geological Society, London, Special*  
810 *Publications*, **259**(1):143-163.
- 811 Chernet, T. (1995). Petrological, geochemical and geochronological investigation of  
812 volcanism in the Northern Main Ethiopian Rift-Southern Afar transition region.  
813 Unpublished Phd. Thesis, Miami University, Ohio, USA.
- 814 Chernet, T., and Hart, W. K. (1999). Petrology and geochemistry of volcanism in the  
815 northern Main Ethiopian Rift-southern Afar transition region. *Acta*  
816 *Vulcanologica*, **11**:21-42.
- 817 Chorowicz, J. (2005). The east African rift system. *Journal of African Earth Sciences*,  
818 **43**(1):379-410.
- 819 Corti, G. (2009). Continental rift evolution: from rift initiation to incipient break-up in the  
820 Main Ethiopian Rift, East Africa. *Earth-Science Reviews*, **96**(1):1-53.
- 821 Cross, C. W., Iddings, J. P., Pirsson, L. V., and Washington, H. S. (1903). *Quantitative*  
822 *classification of igneous rocks*, Univ. Chicago Press.
- 823 Daly, R. A. (1925). The geology of Ascension island. In *Proceedings of the American*  
824 *Academy of Arts and Sciences*. American Academy of Arts and Sciences, **60**(1):3-80.
- 825 Daly, E., Keir, D., Ebinger, C., Stuart, G., Bastow, I., and Ayele, A. (2008). Crustal  
826 tomographic imaging of a transitional continental rift: the Ethiopian rift. *Geophysical*  
827 *Journal International*, **172**(3):1033-1048.
- 828 Damte, A., Boccaletti M., Mazzuoli R, Assefa, G., and Tortorici L. (1992). Geological map  
829 of the Nazareth Dera Region (Main Ethiopian Rift). Scale 1:50,000. S.E.L.C.A.,  
830 Florence, Italy.
- 831 Dugda, M., Nyblade, A., and Julia, J. (2007). Thin lithosphere beneath the Ethiopian Plateau  
832 revealed by a joint inversion of Rayleigh wave group velocities and receiver  
833 functions. *Journal of Geophysical Research: Solid Earth*, (1978–2012) **112**(B8).
- 834 Dugda, M., Nyblade, A., Julia, J., Langston, C., Ammon, C., and Simiyu, S. (2005). Crustal  
835 structure in Ethiopia and Kenya from receiver function analysis: implications for rift

- 836 development in eastern Africa. *Journal of Geophysical Research: Solid Earth*, (1978–  
837 2012) **110**(B1).
- 838 Dufek, J., and Bachmann, O. (2010). Quantum magmatism: Magmatic compositional gaps  
839 generated by melt-crystal dynamics. *Geology*, **38**(8):687-690.
- 840 Ebinger, C. J., and Casey, M. (2001). Continental breakup in magmatic provinces: An  
841 Ethiopian example. *Geology*, **29**(6):527-530.
- 842 Ebinger, C., Yemane, T., Harding, D., Tesfaye, S., Kelley, S., and Rex, D. (2000). Rift  
843 deflection, migration, and propagation: linkage of the Ethiopian and Eastern rifts,  
844 Africa. *Geological Society of America Bulletin*, **112**(2):163-176.
- 845 Ewart, A., and Griffin, W. (1994). Application of proton-microprobe data to trace-element  
846 partitioning in volcanic rocks. *Chemical Geology*, **117**(1):251-284.
- 847 Fassel, V.A., and Kniseley, R. N. (1974). Inductively coupled plasma. Optical emission  
848 spectroscopy. *Analytical Chemistry*, **46**(13):1110A-1120a.
- 849 Ferla, P., and Meli, C. (2006). Evidence of magma mixing in the ‘Daly Gap’ of alkaline  
850 suites: a case study from the enclaves of Pantelleria (Italy). *Journal of*  
851 *Petrology*, **47**(8):1467-1507.
- 852 Fontijn, K., Elburg, M., Nikogosian, I., van Bergen, M., and Ernst, G. (2013). Petrology and  
853 geochemistry of Late Holocene felsic magmas from Rungwe volcano (Tanzania),  
854 with implications for trachytic Rungwe Pumice eruption dynamics. *Lithos*, **177**:34-53.
- 855 Fontijn, K., McNamara, K., Zafu Tadesse, A., Pyle, D.M., Dessalegn, F., Hutchison, W.,  
856 Mather, T.A., and Yirgu, G. (2018). Contrasting styles of post-caldera volcanism  
857 along the Main Ethiopian Rift: Implications for contemporary volcanic hazards.  
858 *Journal of Volcanology and Geothermal Research*;  
859 <https://doi.org/10.1016/j.jvolgeores.2018.02.001>
- 860 Frey, F. A., Green, D. H., and Roy, S. D. (1978). Integrated models of basalt petrogenesis: a  
861 study of quartz tholeiites to olivine melilitites from south eastern Australia utilizing  
862 geochemical and experimental petrological data. *Journal of petrology*, **19**(3):463-513.
- 863 Furman, T., Bryce, J., Rooney, T., Hanan, B., Yirgu, G., and Ayalew, D. (2006). Heads and  
864 tails: 30 million years of the Afar plume. *Geological Society, London, Special*  
865 *Publications*, **259**(1):95-119.
- 866 Gasparon, M., Innocenti, F., Manetti, P., Peccerillo, A., and Abebe, T. (1993). Genesis of the  
867 Pliocene to Recent bimodal mafic-felsic volcanism in the Debre Zeyt area, central  
868 Ethiopia: volcanological and geochemical constraints. *Journal of African Earth*  
869 *Sciences (and the Middle East)*, **17**(2):145-165.

- 870 Giordano, F., D'Antonio, M., Civetta, L., Tonarini, S., Orsi, G., Ayalew, D., Yirgu, G.,  
871 Dell'Erba, F., Di Vito, M.A., and Isaia, R. (2014). Genesis and evolution of mafic and  
872 felsic magmas at Quaternary volcanoes within the Main Ethiopian Rift: Insights from  
873 Gedemsa and Fanta'Ale complexes. *Lithos*, **188**:130-144.
- 874 Gualda, G. A., Ghiorso, M. S., Lemons, R. V., and Carley, T. L. (2012). Rhyolite-MELTS: a  
875 modified calibration of MELTS optimized for silica-rich, fluid-bearing magmatic  
876 systems. *Journal of Petrology*, **53**(5):875-890.
- 877 Hay, D. E., and Wendlandt, R. F. (1995). The origin of Kenya rift plateau-type flood  
878 phonolites: Results of high-pressure/high-temperature experiments in the systems  
879 phonolite-H<sub>2</sub>O and phonolite-H<sub>2</sub>O-CO<sub>2</sub>. *Journal of Geophysical Research: Solid*  
880 *Earth*, **100**(B1):401-410.
- 881 Hayward, N. and Ebinger, C. (1996). Variations in the along-axis segmentation of the Afar  
882 Rift system. *Tectonics*, **15**(2):244-257.
- 883 Hofmann, A.W. (2003). Sampling mantle heterogeneity through oceanic basalts: isotopes  
884 and trace elements. In: Carlson, R.W. (Ed.), *Treatise on Geochemistry. The Mantle*  
885 *and Core vol. 3*. Elsevier, New York, pp. 61–101.
- 886 Hofmann, A. W., Jochum, K. P., Seufert, M., and White, W. M. (1986). Nb and Pb in oceanic  
887 basalts: new constraints on mantle evolution. *Earth and Planetary science*  
888 *letters*, **79**(1-2):33-45.
- 889 [http://ethiopianrift.igg.cnr.it/utilities\\_MER.html](http://ethiopianrift.igg.cnr.it/utilities_MER.html) retrieved on the date 25-Oct-2016
- 890 Hutchison, W., Mather, T. A., Pyle, D. M., Boyce, A. J., Gleeson, M. L., Yirgu, G, Blundy,  
891 J.D, Ferguson, J.D, Vye-Brown, C., Millar, L.I., Sims, K. W., and Finch, A.A. (2018).  
892 The evolution of magma during continental rifting: New constraints from the isotopic  
893 and trace element signatures of silicic magmas from Ethiopian volcanoes. *Earth and*  
894 *Planetary Science Letters*, **489**:203-218.
- 895 Hutchison, W., Pyle, D.M., Mather, T.A., Yirgu, G., Biggs, J., Cohen, B.E., Barfod, D.N.,  
896 and Lewi, E. (2016). The eruptive history and magmatic evolution of Aluto volcano:  
897 new insights into silicic peralkaline volcanism in the Ethiopian rift. *Journal of*  
898 *Volcanology and Geothermal Research*, **328**:9-33.
- 899 Irvine, T., and Baragar, W. (1971). A guide to the chemical classification of the common  
900 volcanic rocks. *Canadian journal of earth sciences*, **8**(5):523-548.
- 901 Jones, W. B. (1979). Mixed benmoreite/trachyte flows from Kenya and their bearing on the  
902 Daly Gap. *Geological Magazine*, **116**(6):487-489.



- 903 Keir, D., Ebinger, C. J., Stuart, G. W., Daly, E., and Ayele, A. (2006). Strain accommodation  
904 by magmatism and faulting as rifting proceeds to breakup: Seismicity of the northern  
905 Ethiopian rift. *Journal of Geophysical Research: Solid Earth*, **111**(B5).
- 906 Keranen, K., Klemperer, S. L., Gloaguen, R., and Group, E. W. (2004). Three-dimensional  
907 seismic imaging of a protoridge axis in the Main Ethiopian rift. *Geology*, **32**(11):949-  
908 952.
- 909 Keranen, K. M., Klemperer, S. L., Julia, J., Lawrence, J. F., and Nyblade, A. A. (2009). Low  
910 lower crustal velocity across Ethiopia: Is the Main Ethiopian Rift a narrow rift in a hot  
911 craton? *Geochemistry, Geophysics, Geosystems*, **10**(5).
- 912 Kieffer, B., Arndt, N., Lapierre, H., Bastien, F., Bosch, D., Pecher, A., Yirgu, G., Ayalew, D.,  
913 Weis, D., Jerram, D. A., Keller, F., and Meugniot, C. (2004). Flood and shield basalts  
914 from Ethiopia: Magmas from the African superswell. *Journal of Petrology*,  
915 **45**(4):793-834.
- 916 Kushiro, I. (1996). Partial melting of a fertile mantle peridotite at high pressures: an  
917 experimental study using aggregates of diamond. *Earth processes: Reading the*  
918 *isotopic code*, 109-122.
- 919 Le Bas, M. J., Le Maitre, R., Streckeisen, A., and Zanettin, B. (1986). A chemical  
920 classification of volcanic rocks based on the total alkali-silica diagram. *Journal of*  
921 *Petrology*, **27**(3):745-750.
- 922 Lowenstern, J. B., Charlier, B. L. A., Clyne, M. A., and Wooden, J. L. (2006). Extreme U-  
923 Th disequilibrium in rift-related basalts, rhyolites and granophyric granite and the  
924 timescale of rhyolite generation, intrusion and crystallization at Alid Volcanic Center,  
925 Eritrea. *Journal of Petrology*, **47**(11):2105-2122.
- 926 Macdonald, R. (1974). Nomenclature and petrochemistry of the peralkaline oversaturated  
927 extrusive rocks. *Bulletin Volcanologique*, **38**(2):498-516.
- 928 Macdonald, R., Bagiński, B., Ronga, F., Dzierżanowski, P., Lustrino, M., Marzoli, A., and  
929 Melluso, L. (2012). Evidence for extreme fractionation of peralkaline silicic magmas,  
930 the Boseti volcanic complex, Main Ethiopian Rift. *Mineralogy and Petrology*, **104**(3-  
931 4):163-175.
- 932 Macdonald, R., Belkin, H. E., Fitton, J. G., Rogers, N. W., Nejbirt, K., Tindle, A. G., and  
933 Marshall, A. S. (2008). The roles of fractional crystallization, magma mixing, crystal  
934 mush remobilization and volatile-melt interactions in the genesis of a young basalt-  
935 peralkaline rhyolite suite, the Greater Olkaria Volcanic Complex, Kenya Rift  
936 Valley. *Journal of Petrology*, **49**(8):1515-1547.

- 937 Macgregor, D. (2015). History of the development of the East African Rift System: A series  
938 of interpreted maps through time. *Journal of African Earth Sciences*, **101**:232-252.
- 939 Mackenzie, G., Thybo, H., and Maguire, P. (2005). Crustal velocity structure across the Main  
940 Ethiopian Rift: results from two-dimensional wide-angle seismic modelling.  
941 *Geophysical Journal International*, **162**(3):994-1006.
- 942 Mahatsente, R., Jentzsch, G., and Jahr, T. (1999). Crustal structure of the Main Ethiopian Rift  
943 from gravity data: 3-dimensional modeling. *Tectonophysics*, **313**(4):363-382.
- 944 Maguire, P. K. H., Keller, G. R., Klemperer, S. L., Mackenzie, G. D., Keranen, K., Harder,  
945 S., O'Reilly, B., Thybo, H., Asfaw, L., Khan, M.A., and Amha, M. (2006). Crustal  
946 structure of the northern Main Ethiopian Rift from the EAGLE controlled-source  
947 survey; a snapshot of incipient lithospheric break-up. *Geological Society, London,*  
948 *Special Publications*, **259**(1):269-292.
- 949 Marsh, B. D. (1981). On the crystallinity, probability of occurrence, and rheology of lava and  
950 magma. *Contributions to Mineralogy and Petrology*, **78**(1):85-98.
- 951 Mazzarini, F., Le Corvec, N., Isola, I., and Favalli, M. (2016). Volcanic field elongation, vent  
952 distribution, and tectonic evolution of a continental rift: The Main Ethiopian Rift  
953 example. *Geosphere*, **12**(3):706-720
- 954 McDonough, W. F., and Sun, S.S. (1995). The composition of the Earth. *Chemical Geology*,  
955 **120**(3):223-253.
- 956 Mohr, P. (1971). Ethiopian Rift and plateaus: some volcanic petrochemical differences.  
957 *Journal of Geophysical Research*, **76**(8):1967-1984.
- 958 Mohr, P. (1983a). The Morton-Black hypothesis for the thinning of continental crust revisited  
959 in western Afar. *Tectonophysics*, **94**(1):509-528.
- 960 Mohr, P. (1983b). Volcanotectonic aspects of Ethiopian rift evolution. *Bulletin Centre*  
961 *Recherches Elf Aquitaine Exploration Production*, **7**:175-189.
- 962 Mohr, P., and Zanettin, B. (1988). The Ethiopian flood basalt province. **In:** *Continental flood*  
963 *basalts*, pp. 63-110: Springer, Netherlands.
- 964 Montaser, A. (1998). *Inductively coupled plasma mass spectrometry*. John Wiley and Sons.
- 965 Morley, C. (1999). Tectonic evolution of the East African Rift System and the modifying  
966 influence of magmatism. *Acta vulcanologica*, **11**:1-20.
- 967 Morton, W. (1979). Riftward younging of volcanic units in the Addis Ababa region,  
968 Ethiopian rift valley. *Nature*, **280**:284-288.



- 969 Neumann, H., Mead, J., and Vitaliano, C. J. (1954). Trace element variation during fractional  
970 crystallization as calculated from the distribution law. *Geochimica et Cosmochimica*  
971 *Acta*, **6**(2-3):90-99.
- 972 Peccerillo, A., Barberio, M., Yirgu, G., Ayalew, D., Barbieri, M., and Wu, T. (2003).  
973 Relationships between mafic and peralkaline silicic magmatism in continental rift  
974 settings: a petrological, geochemical and isotopic study of the Gedemsa volcano,  
975 central Ethiopian rift. *Journal of Petrology*, **44**(11).
- 976 Peccerillo, A., Donati, C., Santo, A., Orlando, A., Yirgu, G., and Ayalew, D. (2007).  
977 Petrogenesis of silicic peralkaline rocks in the Ethiopian rift: geochemical evidence  
978 and volcanological implications. *Journal of African Earth Sciences*, **48**(2):161-173.
- 979 Pik, R., Deniel, C., Coulon, C., Yirgu, G., and Marty, B. (1999). Isotopic and trace element  
980 signatures of Ethiopian flood basalts: evidence for plume–lithosphere  
981 interactions. *Geochimica et Cosmochimica Acta*, **63**(15):2263-2279.
- 982 Rampey, M.L., Oppenheimer, C., Pyle, D.M., and Yirgu, G., (2010). Caldera-forming  
983 eruptions of the Quaternary Kone Volcanic Complex, Ethiopia. *Journal of African*  
984 *Earth Sciences*, **58**(1):51-66.
- 985 Rapprich, V., Žáček, V., Verner, K., Erban, V., Goslar, T., Bekele, Y., Legesa, F., Hroch, T.,  
986 and Hejtmánková, P. (2016). Wendo Koshe Pumice: the latest Holocene silicic  
987 explosive eruption product of the Corbetti Volcanic System (Southern  
988 Ethiopia). *Journal of Volcanology and Geothermal Research*, **310**:159-171.
- 989 Ring, U. (2014). The East African Rift System. *Austrian J Earth Sci*, **107**(1):132-146.
- 990 Ronga, F., Lustrino, M., Marzoli, A., and Melluso, L. (2010). Petrogenesis of a basalt-  
991 comendite-pantellerite rock suite: the Boseti Volcanic Complex (Main Ethiopian  
992 Rift). *Mineralogy and Petrology*, **98**(1-4):227-243.
- 993 Rooney, T. (2010). Geochemical evidence of lithospheric thinning in the southern Main  
994 Ethiopian Rift. *Lithos*, **117**(1):33-48.
- 995 Rooney, T. (2017). The Cenozoic magmatism of East-Africa: Part I — Flood basalts and  
996 pulsed magmatism. *Lithos*, **286–287**:264-301.
- 997 Rooney, T. O., Bastow, I. D., and Keir, D. (2011). Insights into extensional processes during  
998 magma assisted rifting: Evidence from aligned scoria cones. *Journal of Volcanology*  
999 *and Geothermal Research*, **201**(1-4):83-96.
- 1000 Rooney, T., Furman, T., Bastow, I., Ayalew, D., and Yirgu, G. (2007). Lithospheric  
1001 modification during crustal extension in the Main Ethiopian Rift. *Journal of*  
1002 *Geophysical Research: Solid Earth*, **112**(B10).

- 1003 Rooney, T. O., Nelson, W. R., Dosso, L., Furman, T., and Hanan, B. (2014). The role of  
1004 continental lithosphere metasomes in the production of HIMU-like magmatism on the  
1005 northeast African and Arabian plates. *Geology*, **42**(5):419-422.
- 1006 Rudnick, R. L., and Gao, S. (2003). Composition of the continental crust. In *Treatise on*  
1007 *geochemistry* (eds. H.D. Holland and K.K. Turekian), Elsevier-Pergamon,  
1008 Oxford, **3**:659.
- 1009 Saria, E., Calais, E., Stamps, D.S., Delvaux, D., and Hartnady, C.J.H. (2014). Present-day  
1010 kinematics of the East African Rift. *Journal of Geophysical Research: Solid Earth*,  
1011 **119**(4):3584-3600.
- 1012 Siegburg, M., Gernon, T. M., Bull, J. M., Keir, D., Barfod, D. N., Taylor, R. N., Abebe, B.,  
1013 and Ayele, A. (2018). Geological evolution of the Boset-Bericha Volcanic Complex,  
1014 Main Ethiopian Rift:  $^{40}\text{Ar}/^{39}\text{Ar}$  evidence for episodic Pleistocene to Holocene  
1015 volcanism. *Journal of Volcanology and Geothermal Research*, **351**:115-133.
- 1016 Stormer Jr, J. C., and Nicholls, J. (1978). XLFRAC: a program for the interactive testing of  
1017 magmatic differentiation models. *Computers & Geosciences*, **4**(2):143-159.
- 1018 Taylor SR., and McLennan SM. (1985). *The continental crust: its composition and evolution*.  
1019 Blackwell Scientific Publication, Carlton, 312 p.
- 1020 Teklay, M., Kröner, A., Mezger, K., and Oberhänsli, R. (1998). Geochemistry, Pb-Pb single  
1021 zircon ages and Nd-Sr isotope composition of Precambrian rocks from southern and  
1022 eastern Ethiopia: implications for crustal evolution in East Africa. *Journal of African*  
1023 *Earth Sciences*, **26**(2):207-227.
- 1024 Thy, P., Beard, J. S. and Lofgren, G. E. (1990). Experimental constraints on the origin of  
1025 Icelandic rhyolites. *The Journal of Geology*, **98**(3):417-421.
- 1026 Trua, T., Deniel, C., and Mazzuoli, R. (1999). Crustal control in the genesis of Plio-  
1027 Quaternary bimodal magmatism of the Main Ethiopian Rift (MER): geochemical and  
1028 isotopic (Sr, Nd, Pb) evidence. *Chemical Geology*, **155**(3):201-231.
- 1029 Weissel, J. K., and Karner, G. D. (1989). Flexural uplift of rift flanks due to mechanical  
1030 unloading of the lithosphere during extension. *J. geophys. Res*, **94**(B10):13919-13950.
- 1031 Woldegabriel, G., Aronson, J. L., and Walter, R. C. (1990). Geology, geochronology, and rift  
1032 basin development in the central sector of the Main Ethiopia Rift. *Geological Society*  
1033 *of America Bulletin*, **102**(4):439-458.
- 1034 Wolfenden, E., Ebinger, C., Yirgu, G., Deino, A., and Ayalew, D. (2004) Evolution of the  
1035 northern Main Ethiopian Rift: Birth of a Triple Junction. *Earth and Planetary Science*  
1036 *Letters*, **224**:213-228.

1037 **Figure Captions**

1038

1039 **Figure 1:** Digital elevation model showing the north-central segment of the MER and its  
1040 bounding plateau (Eastern and Western Plateau). The fault lines are from  
1041 [http://ethiopianrift.igg.cnr.it/utilities\\_MER.html](http://ethiopianrift.igg.cnr.it/utilities_MER.html).

1042

1043 **Figure 2:** (A) Sketch geological map of the study area (modified after Damte et al., 1992).  
1044 (B) Geological cross-section along A-A' traverse line. The scale for the vertical axis in the  
1045 geological cross-section is labeled in meters. The vertical scale is two times exaggerated. (C)  
1046 Composite stratigraphy of BVC.

1047

1048 **Figure 3:** Pumice flow exposures at base of the Dabe section (A) and the southern tip of  
1049 Boku ridge (B). Note that in figure "A" the lithic fragments are rhyolite and obsidian lava  
1050 (indicated by an arrow). On "B" the outcrop shows intercalation of ash flow with pumice  
1051 flow layers underlain by basaltic lava flows (Qbl). Pumice fall is exposed on the Dabe section  
1052 interbedded between ash flow deposits. C) Dabe section showing interbedding of pumice fall  
1053 layer between ash flows.

1054

1055 **Figure 4:** Litho-stratigraphic correlation between BVC and Nazret-Dera area. The Nazret-  
1056 Dera area volcanic stratigraphy is after Boccaletti et al. (1999).

1057

1058 **Figure 5:** TAS diagram for BVC after Le Bas et al. (1986). The dashed line separates the  
1059 alkaline from subalkaline series (Irvine and Baragar, 1971). The major element data are  
1060 normalized under volatile-free base out of 100%. The grey field shows previously published  
1061 whole-rock chemical data for other MER volcanoes (Rapprich et al., 2016; Giordano et al.,  
1062 2014; Boccaletti et al., 1995; Chernet and Hart, 1999; Gasparon et al., 1993; Peccerillo et al.,  
1063 2003; 2007; Ronga et al., 2010; Rooney 2010; Rooney et al., 2011; Rooney et al., 2014;  
1064 Rooney et al., 2007; Hutchison et al., 2016). The grey field encloses predominant mafic and  
1065 felsic rocks with rare rocks of intermediate composition, specifically at Boset and Aluto  
1066 (Ronga et al., 2010; Hutchison et al., 2016; 2018; Seigburg et al., 2018).

1067

1068 **Figure 6:** A) Classification of silicic volcanic products from BVC after Le Bas et al. (1986).  
1069 B) Classification diagram of peralkaline silicic rocks (after Macdonald, 1974).

1070

1071 **Figure 7:** Selected major element Harker diagrams of BVC whole-rock compositions.

1072

1073 **Figure 8:** Selected trace element variation diagrams against SiO<sub>2</sub>.

1074

1075 **Figure 9:** Selected trace element plot against Zr.

1076

1077 **Figure 10:** (A) REE variation diagram of representative samples from mafic and silicic  
1078 rocks. The concentrations are normalized to chondrite values (Boynnton, 1984). (B) Multi-  
1079 element spider diagram of representative mafic and silicic rocks of BVC. The concentrations  
1080 are normalized to the primordial mantle value determined by McDonough and Sun (1995).

1081

1082 **Figure 11:** La/Nb (A) and Th/Ta against SiO<sub>2</sub> (B) diagrams of rock samples collected from  
1083 Boku volcano and adjacent volcanoes (Gedemsa and Fenta'Ale after Giordano et al., 2014).  
1084 (C) and (D) plots show the trace element ratios (Rb/Nb and Rb/Zr) of BVC samples  
1085 compared with Ethiopian flood basalt (EFB) and Precambrian rocks (M-BR: metamorphic  
1086 basement rock and C-BR: crystallized or plutonic basement rock). The data in diagram "C"  
1087 and "D" is adopted from Alene et al. (2000), Teklay et al. (1998), Asrat and Barbey (2003)  
1088 and Kieffer et al. (2004).

1089

1090 **Figure.12:** (A) Rb vs. Sr diagram to highlight the degree of variations in incompatible versus  
1091 compatible element concentrations. (B) Trace element modeling. The partition coefficients  
1092 used in the model for Sr and Rb are adopted from Ewart and Griffin (1994). Fractional  
1093 crystallization model by applying the equation of Neuman et al. (1954) to see trace element at  
1094 80% fractionation displayed on REE (C) and spidergram (D) plot.

1095

1096 **Figure 13.** Different graphs illustrating petrogenetic modelling of peralakkaline silicic rocks.  
1097 A) SiO<sub>2</sub> against temperature graph for selected different pressure conditions. B) The  
1098 classification plot after LeBas et al. (1986) of the remaining melt at different pressure  
1099 conditions. C) Mass proportion of different mineral phases crystallizing in function of  
1100 temprature at 0.6 kbar. D) Schematic diagram illustrating progressive evolution of mafic  
1101 melts sourced from the upper mantle. Depth extent of the partial melting and depth of melt  
1102 ponding at shallow crust levels is inferred from geophysical and geochemical studies (e.g.  
1103 Ayalew and Gibson, 2009; Dugda et al., 2005; Rooney et al., 2011; Keranen et al., 2009;  
1104 Keranen et al., 2004).

1105 **Tables**

1106 **Table 1:** Geochemical data of BVC samples; the major element (including LOI) and trace  
 1107 element concentrations are expressed in wt% and ppm respectively. The major element data  
 1108 is normalized to 100% at volatile-free base. AI\*\* is  
 1109 Agpaitic index calculated as molecular  $(\frac{Al_2O_3}{Na_2O+K_2O})$  and L.D\* is the ICP-MS limit of  
 1110 detection for different trace elements. The CIPW norm values for the selected minerals are  
 1111 the percentage calculated from the chemical analysis based on the rule of norm calculation  
 1112 after Cross et al. (1903).

1113

Sample	NB-01	NB-07	NB-02	NB-03	NB-08	NB-05	NB-06	NB-04
Lithology	Basalt	Basalt	Basalt	Scoria	Scoria	Basalt	Basalt	Basalt
<b>ICP-OES (wt%)</b>								
SiO <sub>2</sub>	45.43	46.62	47.3	47.58	47.93	48.13	49.29	49.37
TiO <sub>2</sub>	2.19	2.20	2.29	2.01	1.69	1.97	1.93	1.90
Al <sub>2</sub> O <sub>3</sub>	16.81	14.89	15.84	15.44	14.68	15.84	17.26	15.79
FeO <sub>t</sub>	11.46	11.04	10.98	10.61	9.93	10.63	11.26	10.53
MnO	0.19	0.18	0.19	0.18	0.17	0.18	0.18	0.18
MgO	8.81	9.02	7.81	8.81	9.77	7.9	5.79	7.08
CaO	10.52	11.17	10.73	10.52	11.48	10.22	9.84	9.65
Na <sub>2</sub> O	2.52	2.65	2.66	2.67	2.3	2.75	3.11	3.00
K <sub>2</sub> O	0.46	0.59	0.67	0.67	0.58	0.86	0.92	1.00
P <sub>2</sub> O <sub>5</sub>	0.33	0.42	0.35	0.36	0.38	0.35	0.29	0.34
Total	98.72	98.78	98.82	98.85	98.91	98.83	98.87	98.84
LOI	1.76	0.16	1.79	0.44	1.52	0.64	1.37	0.26
<b>Norm (wt %)</b>								
Quartz								
Albite	18.13	18.76	22.29	22.4	19.46	23.27	26.32	25.38
Diopside	13.99	21.21	17.98	17.92	21.7	16.69	13.87	15.88
Hypersthene					2.74	1.37	4.47	4.92
Olivine	24.05	21.21	20.03	21.66	19.48	19.54	14.05	15.72
Nepheline	1.73	1.98	0.12	0.1				
Acmite								
AI**								
<b>ICP-MS (ppm)</b>								
Be	1.121	0.779	1.051	0.985	0.886	0.963	1.082	1.126
Sc	34.86	34.48	32.87	32.89	33.57	32.95	30.33	29.51
V	216	284.1	283.9	263.2	233.6	263.1	266.8	238.6

Cr	368.6	581.3	391.8	392.2	573.8	392.6	157.7	263.2
Co	49.62	49.35	46.66	48.33	48.12	47.28	37.91	43.08
Ni	87.92	143.4	114.6	75.11	153.7	72.93	30.69	53.49
Cu	51.92	72.91	76.48	37.62	89.72	36.28	25.52	37.22
Zn	109.8	97.09	116.2	113	85.96	101.9	97.41	107.1
Rb	3.073	6.691	7.675	10.75	10.62	12.21	13.88	15.82
Sr	433.8	447	441.7	455.9	346.5	441.5	454.7	476.3
Y	23.21	21.76	19.59	20.86	16.98	21.29	21.78	23.15
Zr	133.6	107.6	115.3	124.1	93.79	124.7	127.1	137.7
Nb	23.72	18.45	17.79	21.97	14.41	21.95	20.64	20.11
Sn	1.667	1.351	1.732	1.394	1.254	1.407	1.516	1.815
Cs	<L.D.*	<L.D.	0.023	0.097	0.018	<L.D.	<L.D.	0.129
Ba	254.1	267.1	257.8	250.6	189.2	323.4	268.9	458.6
La	21.27	17.52	15.69	19.11	12.2	19.78	18.35	21.17
Ce	43.67	36.59	34.42	41.31	27.42	41.63	38.98	42.95
Pr	5.746	5.008	4.536	5.278	3.665	5.475	5.142	5.668
Nd	23.92	21.35	19.36	22.18	15.88	22.66	21.24	23.36
Sm	5.329	4.866	4.443	4.877	3.708	4.972	4.703	5.177
Eu	1.855	1.767	1.559	1.703	1.314	1.716	1.653	1.84
Gd	4.901	4.678	4.229	4.5	3.537	4.575	4.382	4.808
Tb	0.746	0.693	0.635	0.678	0.537	0.684	0.677	0.717
Dy	4.49	4.142	3.802	4.071	3.285	4.113	4.087	4.331
Ho	0.908	0.833	0.771	0.822	0.664	0.827	0.832	0.876
Er	2.327	2.084	1.951	2.065	1.67	2.111	2.149	2.238
Tm	0.31	0.281	0.265	0.285	0.232	0.286	0.303	0.308
Yb	2.072	1.799	1.735	1.872	1.507	1.89	1.991	2.011
Lu	0.319	0.271	0.259	0.285	0.233	0.284	0.302	0.306
Hf	3.506	2.822	3.02	3.315	2.5	3.312	3.436	3.642
Ta	1.809	1.42	1.351	1.666	1.104	1.667	1.601	1.539
Pb	2.53	2.1306	3.3679	2.5829	2.2527	2.7221	2.5731	4.2856
Th	2.231	1.572	1.651	2.134	1.355	2.187	2.391	2.576
U	0.211	0.291	0.328	0.514	0.383	0.377	0.4	0.674

1114

1115

1116

1117

1118

1119

1120

1121 Table 1 continued

Sample	NB-11	NB-12	NB-10	NB-13	NB-16	NB-15	NB-14	NB-09
Lithology	Rhyolite	Rhyolite	Rhyolite	Rhyolite	Rhyolite	Rhyolite	Rhyolite	Rhyolite
<b>ICP-OES (wt %)</b>								
SiO <sub>2</sub>	70.23	70.9	71.12	71.65	73.16	73.3	74.7	75.45
TiO <sub>2</sub>	0.5	0.44	0.44	0.42	0.39	0.19	0.26	0.19
Al <sub>2</sub> O <sub>3</sub>	11.53	11.02	11.61	10.59	9.97	13.68	9.47	10.88
FeO <sub>t</sub>	5.62	5.76	6.46	5.86	6.34	2.29	5.17	4.09
MnO	0.31	0.33	0.25	0.38	0.3	0.02	0.17	0.10
MgO	0.25	0.13	0.10	0.19	0.07	0.07	0.07	0.05
CaO	0.34	0.34	0.15	0.44	0.33	0.18	0.29	0.12
Na <sub>2</sub> O	5.83	5.85	4.22	5.19	4.22	4.91	4.88	3.8
K <sub>2</sub> O	4.75	4.59	4.92	4.64	4.52	5.1	4.43	4.87
P <sub>2</sub> O <sub>5</sub>	< L.D.	< L.D.	< L.D.	< L.D.	< L.D.	< L.D.	< L.D.	< L.D.
Total	99.36	99.36	99.27	99.36	99.30	99.74	99.44	99.55
LOI	0.65	0.43	1.53	0.81	1.52	0.88	0.73	0.85
<b>Norm (wt %)</b>								
Quartz	22.19	24.45	24.03	26.74	31.02	23.04	34.49	32.97
Albite	32.86	31.13	32.33	28.64	26.12	41.55	24.05	28.85
Diopside	1.56	1.55	0.7	2	1.51	0.66	1.29	0.54
Hypersthene	9.87	9.96	11.47	10.18	10.93	3.74	8.87	7.22
Olivine								
Nepheline								
Acmite	14.51	16.18	2.98	13.46	8.46		15.19	2.91
Al	1.09	1.06	1.27	1.08	1.14	1.37	1.02	1.26
<b>ICP-MS (ppm)</b>								
Be	4.873	5.02	5.052	4.647	5.07	3.843	8.043	6.035
Sc	8.19	6.08	5.47	5.13	< L.D.	3.61	< L.D.	< L.D.
V	2.861	1.434	1.863	1.608	0.955	3.992	2.037	4.532
Cr	26.87	17.13	19.83	63.05	15.31	31.35	54.76	24.92
Co	0.332	0.209	0.274	0.365	0.152	0.269	0.365	0.386
Ni	< L.D.	< L.D.	< L.D.	< L.D.	< L.D.	< L.D.	< L.D.	< L.D.
Cu	< L.D.	< L.D.	< L.D.	< L.D.	< L.D.	< L.D.	13.4	< L.D.
Zn	197.9	211.2	192.9	215.7	245.8	87.97	261	176.4
Rb	109.4	107.9	118	118.1	131.1	129	199.1	197.5
Sr	7.062	5.131	8.924	13.84	5.727	12.16	7.829	8.33
Y	55.61	86.34	97.45	64.75	60.53	45.96	89.1	97.57
Zr	662.3	660.4	729.7	684.7	791.4	557.4	958.5	980
Nb	86.59	86.68	94.61	87.79	108.4	57.02	145.6	108.4
Sn	5.925	6.109	6.956	6.209	7.852	5.968	10.23	10.42



Cs	0.659	0.88	0.175	0.439	0.319	0.615	1.442	0.402
Ba	374.1	267.9	228.6	348	280.5	345.5	26.74	46.5
La	75.43	90.7	117.6	76.06	68.48	66.12	90.46	75.94
Ce	160.6	158.4	202.1	199.8	215.1	95.39	219	234.1
Pr	20.12	21.03	29.32	19.73	18.98	16.22	19.15	20.8
Nd	74.51	78.73	109.1	74.05	69.12	57.06	68.38	76.43
Sm	14.82	15.88	20.96	14.83	14.01	10.55	13.78	18.23
Eu	3.383	3.626	4.475	3.262	2.943	0.899	1.494	1.438
Gd	11.83	14.47	17.03	12.59	11.4	8.066	12.96	16.94
Tb	1.925	2.363	2.832	2.057	2.012	1.342	2.244	2.983
Dy	11.82	14.9	17.98	12.89	13.18	8.343	15.11	19.34
Ho	2.338	3.13	3.76	2.682	2.786	1.75	3.292	4.064
Er	6.19	8.348	10.03	7.218	7.881	4.901	9.104	10.88
Tm	0.937	1.233	1.461	1.058	1.217	0.746	1.369	1.634
Yb	6.539	8.49	9.846	7.132	8.716	5.249	9.585	11.22
Lu	1.047	1.338	1.519	1.124	1.347	0.83	1.522	1.684
Hf	15.97	15.8	17.39	16.56	21.41	14.12	26.69	27.19
Ta	6.481	6.426	6.952	6.663	8.067	4.473	10.49	8.431
Pb	15.2845	13.3516	17.598	15.947	21.7491	13.2812	27.5783	28.9164
Th	12.92	12.62	13.92	13.82	16.98	14.09	24.33	21.85
U	1.618	1.563	0.971	2.525	0.868	2.576	1.126	1.691

1122

1123

1124 Table 1 continued

Sample	NB-23	NB-24	NB-20	NB-21	NB-19	NB-22	NB-18	NB-17
Lithology	Ignimbrite	Ignimbrite	Obsidian	Obsidian	Obsidia	Obsidian	Rhyolite	Rhyolite
	e	e			n			
<b>ICP-OES (wt%)</b>								
SiO <sub>2</sub>	68.43	70.27	70.51	70.65	70.86	71.9	73.13	75.4
TiO <sub>2</sub>	0.79	0.5	0.50	0.48	0.48	0.42	0.19	0.20
Al <sub>2</sub> O <sub>3</sub>	12.87	10.7	10.87	11.15	11.19	10.45	13.66	10.96
FeO <sub>t</sub>	5.18	5.91	5.73	5.45	5.48	5.86	2.32	4.08
MnO	0.23	0.34	0.31	0.30	0.30	0.32	0.07	0.04
MgO	0.79	0.42	0.20	0.20	0.20	0.09	0.10	0.06
CaO	1.08	0.84	0.30	0.30	0.30	0.31	0.21	0.22
Na <sub>2</sub> O	5.71	5.78	6.40	6.37	6.38	5.25	4.94	3.53
K <sub>2</sub> O	4.36	4.59	4.53	4.53	4.53	4.76	5.11	5.04
P <sub>2</sub> O <sub>5</sub>	< L.D.	< L.D.	< L.D.	< L.D.	< L.D.	< L.D.	< L.D.	< L.D.
Total	99.44	99.35	99.35	99.43	99.72	99.36	99.73	99.57
LOI	0.79	1.60	-0.05	0.08	0.00	2.51	0.44	1.74



<b>Norm (wt%)</b>								
Quartz	15.86	23.77	24.03	23.6	23.66	27.61	22.56	32.79
Albite	41.92	29.48	30.69	30.69	32.34	27.25	41.8	28.31
Diopside	4.75	3.73	1.38	1.38	1.39	1.42	0.98	0.98
Hypersthene	8.14	9.74	10.04	9.54	9.59	10.13	3.81	6.86
Olivine								
Nepheline								
Acmite	5.63	17.11	18.43	17.53	17.62	15.43		1.37
Al	1.28	1.03	1	1.02	1.03	1.04	1.36	1.29
<b>ICP-MS (ppm)</b>								
Be	4.042	4.636	4.429	4.54	4.499	5.091	4.175	5.267
Sc	13.25	7.35	7.94	7.93	8.06	4.91	3.8	< L.D.
V	36.27	2.962	1.709	1.616	1.67	0.66	5.152	6.634
Cr	59.66	31.66	22.78	30.66	39.83	19.61	50.92	24.96
Co	4.624	0.313	0.225	0.127	0.225	0.073	0.405	0.119
Ni	< L.D.	< L.D.	< L.D.	< L.D.	< L.D.	< L.D.	< L.D.	< L.D.
Cu	6.245	< L.D.	< L.D.	9.905	< L.D.	< L.D.	< L.D.	< L.D.
Zn	180.3	212.5	208.9	199.4	193.2	222.3	83.54	189.7
Rb	90.87	106.1	106.5	108.2	103.7	122	127.3	195.3
Sr	56.11	13.05	2.189	2.411	2.306	3.723	11.73	13.53
Y	71.28	77.81	76.57	76.7	73.96	84.69	52.12	96.69
Zr	565	652.2	646.8	644.6	618.2	706.1	544.5	946.2
Nb	75.24	88.16	87.26	86.32	83.17	91.63	55.74	106
Sn	5.007	5.992	6.011	5.991	5.722	6.465	5.018	8.543
Cs	0.95	0.931	1.573	1.559	1.476	1.874	0.751	0.269
Ba	574.6	370.3	333.2	405.9	390.7	293.8	346.4	19.41
La	76.53	101.7	78.91	81.09	75.38	87.64	64.1	106
Ce	144.8	166.5	172.5	175.1	167.9	189.5	133.1	210.5
Pr	18.56	22.66	19.92	20.26	19.4	21.88	15.08	25.72
Nd	69.72	84.3	73.85	76	72.77	83.06	53.64	93.18
Sm	14.32	16.74	15.36	15.34	14.81	17.09	10.24	20.01
Eu	3.116	3.797	3.569	3.562	3.438	3.777	0.853	1.322
Gd	12.35	14.03	13.16	13.33	12.78	14.91	8.541	17.42
Tb	2.068	2.326	2.21	2.214	2.13	2.461	1.4	2.815
Dy	12.86	14.32	13.91	13.92	13.38	15.37	8.83	17.37
Ho	2.737	2.979	2.957	2.932	2.818	3.267	1.877	3.681
Er	7.359	8.081	7.93	7.869	7.621	8.667	5.181	9.896
Tm	1.081	1.188	1.17	1.163	1.101	1.275	0.773	1.451
Yb	7.314	8.12	7.913	7.857	7.441	8.612	5.39	9.737
Lu	1.111	1.232	1.215	1.192	1.144	1.317	0.841	1.471

Hf	13.66	15.96	15.63	15.66	14.98	17.26	13.59	26.18
Ta	5.464	6.487	6.398	6.354	6.076	6.787	4.361	8.117
Pb	12.9708	14.2818	15.3291	15.5061	14.7386	17.1482	13.4227	14.5133
Th	10.07	13.02	12.78	12.68	12.23	14.21	13.67	21.18
U	2.234	2.235	2.982	2.936	2.859	3.218	2.367	2.443

1125

1126 Table 1 continued

Sample	NB-29	NB-27	NB-26	NB-25	NB-30	NB-28
Lithology	Pumice	Pumice	Pumice	Pumice	Pumice	Pumice
<b>ICP-OES (wt%)</b>						
SiO <sub>2</sub>	68.93	70.33	71.59	72.7	73.01	73.09
TiO <sub>2</sub>	0.28	0.45	0.47	0.46	0.44	0.38
Al <sub>2</sub> O <sub>3</sub>	7.75	16.07	11.7	11.46	10.86	10.43
FeO <sub>t</sub>	8.04	3.28	6.52	6.41	6.06	6.04
MnO	0.35	0.07	0.33	0.34	0.33	0.28
MgO	0.22	0.88	0.43	0.21	0.12	0.1
CaO	3.98	1.04	1.14	0.67	0.4	0.5
Na <sub>2</sub> O	5.04	1.74	1.63	2	1.87	1.75
K <sub>2</sub> O	4.52	5.78	5.46	5.04	6.25	6.77
P <sub>2</sub> O <sub>5</sub>	< L.D.	< L.D.	< L.D.	< L.D.	< L.D.	< L.D.
Total	99.11	99.64	99.27	99.29	99.34	99.34
LOI	7.94	9.50	9.08	9.04	7.40	7.03
<b>Norm (wt%)</b>						
Quartz	26.84	32.01	32.67	34.65	32.1	31.12
Albite	14.7	14.72	13.79	16.92	15.82	14.81
Diopside	17.62					1.74
Hypersthene	6.17	7.59	12.89	12.16	11.3	10.31
Olivine						
Nepheline						
Acmite	24.62					
Al	0.81	2.14	1.65	1.63	1.34	1.22
<b>ICP-MS (ppm)</b>						
Be	7.068	4.068	5.187	4.798	4.866	5.373
Sc	< L.D.	5.22	5.55	5.12	4.77	3.01
V	2.439	14.69	1.755	0.707	1.356	1.311
Cr	16.75	13.83	< L.D.	< L.D.	35.46	26.04
Co	0.409	2.303	0.317	0.04	0.248	0.166
Ni	< L.D.	< L.D.	< L.D.	< L.D.	< L.D.	< L.D.
Cu	< L.D.	< L.D.	< L.D.	< L.D.	< L.D.	< L.D.
Zn	334.6	79.04	222.9		217.7	235

Rb	124.6	123.9	198.6	221.4	158.3	178.5
Sr	92.67	117.9	30.25	256	7.489	22.04
Y	136.3	30.72	81.64	52.83	87.5	98.87
Zr	882.5	427.4	722.1	82.59	702.3	713.4
Nb	160.5	41.86	93.56	718.5	89.42	98.76
Sn	9.441	5.412	6.643	93.29	6.449	7.416
Cs	1.189	1.01	2.2	6.577	1.778	1.735
Ba	510.8	447	308.2	2.027	284.9	372
La	131.2	50.43	90.03	282.9	90.11	120.5
Ce	245.4	89.1	194.6	87.62	185.3	222.5
Pr	28.2	10.57	21.91	188.8	21.6	26.53
Nd	108.2	36.8	83.9	21.57	82.06	102
Sm	22.87	6.689	17.41	81.69	16.63	20.87
Eu	5.663	0.859	3.855	16.85	3.729	4.373
Gd	21.26	5.48	15.12	3.738	14.69	18.41
Tb	3.553	0.867	2.482	14.65	2.402	2.957
Dy	22.84	5.409	15.49	2.427	15.09	18.36
Ho	4.926	1.139	3.228	15.17	3.212	3.825
Er	13.16	3.145	8.617	3.194	8.583	10.06
Tm	1.948	0.499	1.275	8.509	1.275	1.459
Yb	13.15	3.502	8.781	1.244	8.548	9.861
Lu	1.959	0.54	1.326	8.521	1.281	1.465
Hf	24.23	11.3	17.42	1.284	16.92	20.21
Ta	11.09	3.726	6.937	17.46	6.669	7.435
Pb	17.337	13.7325	17.6564	6.874	17.0445	19.8169
Th	16.69	14.02	14.68	17.2367	13.96	16.14
U	4.163	2.298	2.933	14.52	3.194	3.314
				3.07		

1127

1128

1129

1130

1131

1132

1133

1134

1135

1136

1137 **Table 2:** Rb/Nb and Rb/Zr values of BVC samples compared to Ethiopian Precambrian rock  
 1138 and flood basalt data. Northern Ethiopia Precambrian rock data after Alene et al. (2000),  
 1139 Southern and Eastern Precambrian metamorphic rock after Teklay et al. (1998) and Konso  
 1140 pluton data from Asrat and Barbey (2003). The flood basalt data is taken from Kieffer et al.  
 1141 (2004).  
 1142

	BVC		Flood Basalt	Northern Ethiopia			Southern and Eastern Ethiopia	
	Basalti	Silici		Basic/Inter mediate	Acidic	Pluton	Metamorphi c rock	Konso Pluton
	c rock	c rock						
<b>Rb/Nb</b>	0	0.13-1.37	0.13-2.16	1-6.33	0-5.56	0.6-12.6	0.2-10.07	1.12-5.81
<b>Rb/Zr</b>	0	0.023-0.21	0.0072-0.32	0.048-0.5	0-0.37	0.27-1.8	0.015-0.59	0.085-0.65

1143

1144

Fig. 1

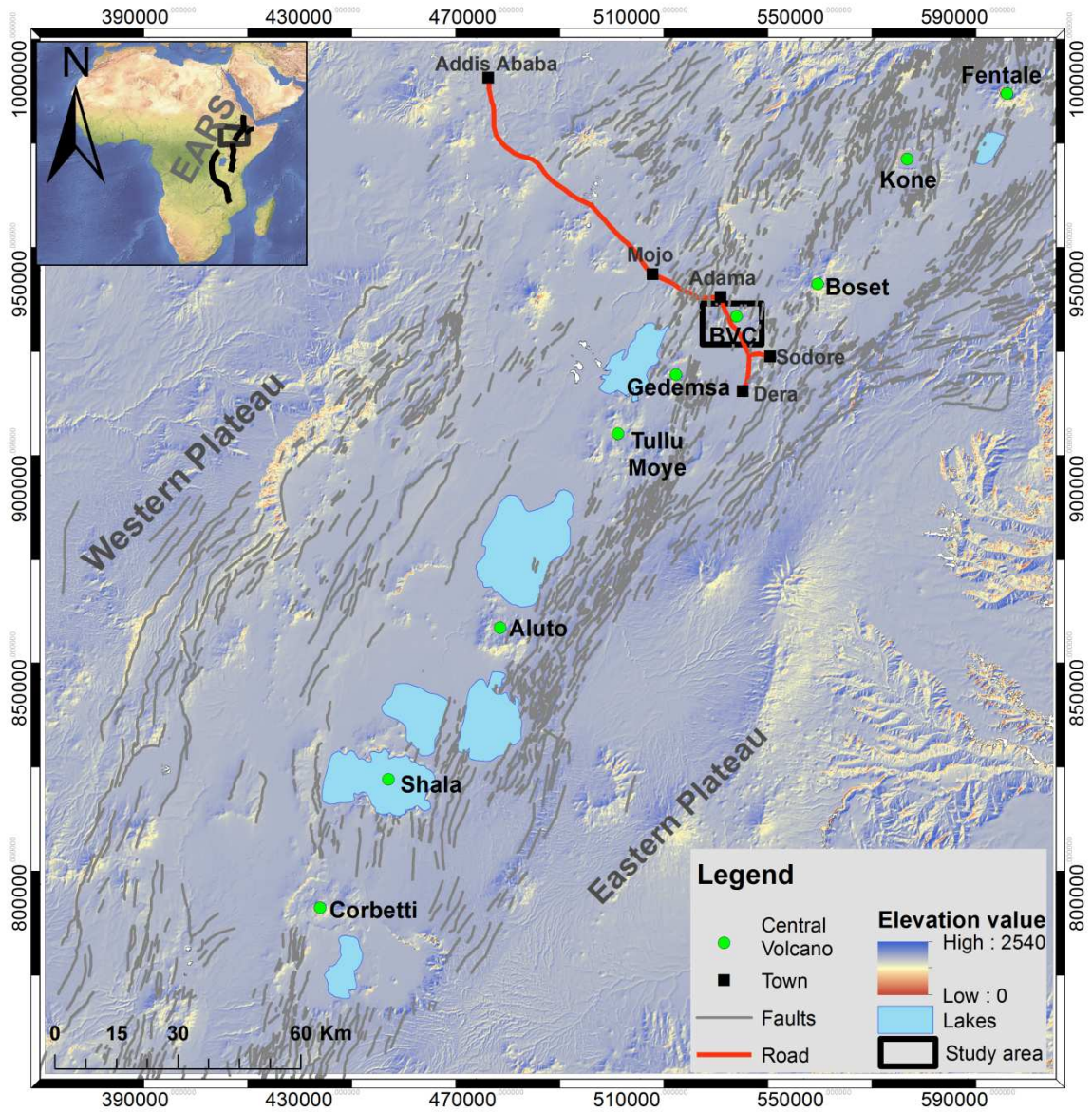
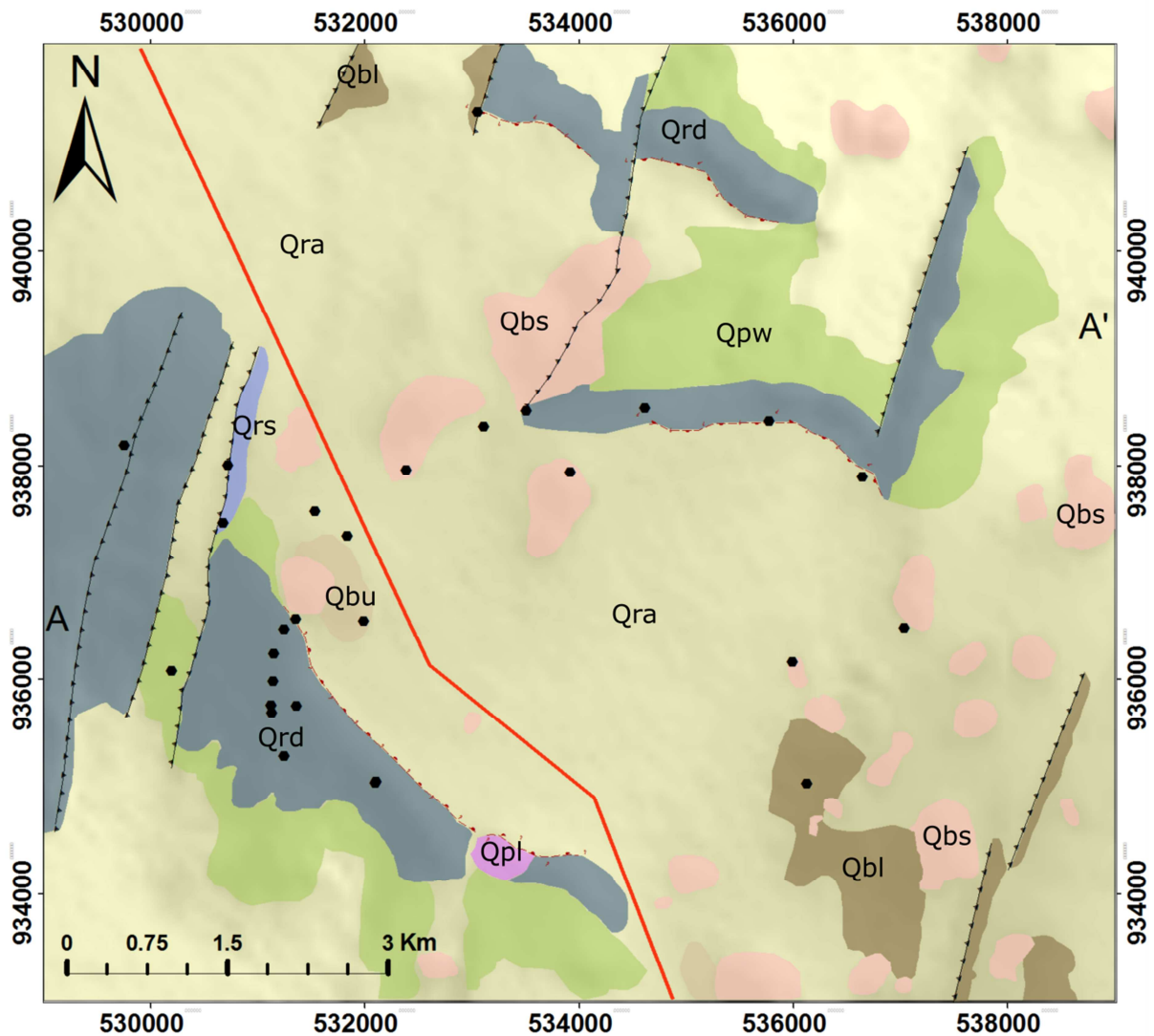


Fig. 2

A)



## Legend

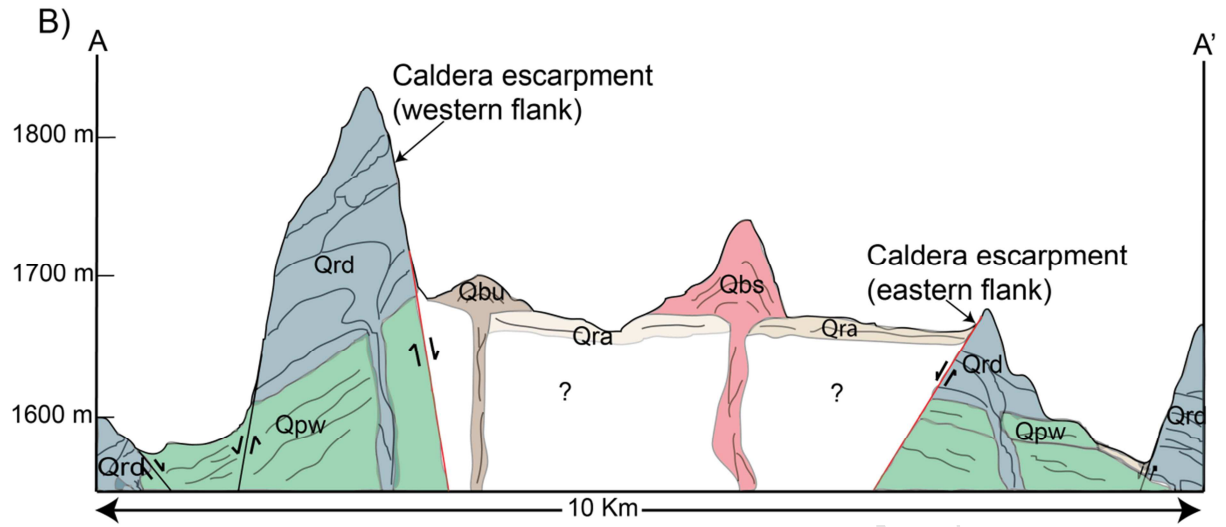
### Symbols

- Geochemical sample points
- ▲--- NNE-SSW trending normal fault
- Ring-normal fault
- Road

### Lithology

- Upper Basaltic Lava Flow (Qbu)
- Basaltic scoria (Qbs)
- Ash flow (Qra)
- Lower Basaltic Lava Flow (Qbl)
- Rhyolitic Lava Dome (Qrd)
- Ash and Pumice Fall (Qpl)
- Pumice Flow (Qpw)
- Rhyolitic Lava Flow (Qrf)







C)

Thickness (m)	Stratigraphy	Stratigraphic units	Geochemical Samples	Characteristics
		Qbu	NB-02 NB-04 NB-05 NB-06	Basalt lava flow: associated to scoria cones. Phyric to Porphyritic in texture dominated by plagioclase feldspar phenocryst.
		Qbs	NB-03 NB-08	Basaltic scoria: black to red in color, form a spatter cone, show graded bedding and associated to Qbu.
		Qra (upper)	NB-29	Ash flow: matrix supported pyroclastics, poorly sorted and intercalated with ash fall and pumice flow.
		Qbl	NB-01 NB-07	Basalt lava flow: Porphyritic in texture with phenocrysts of plagioclase feldspar and olivine dominated.
		Qrd (obsidian flow)	NB-19 NB-20 NB-21 NB-22	Obsidian flow: fragmented nature in the base, well indurated on the top, crystal free and associated to dome forming rhyolite lava.
		Qrd (lava dome)	NB-09 NB-10 NB-11 NB-12 NB-13 NB-15 NB-16	Dome forming rhyolites: capped by ash flow and obsidian flow, hyalopilitic in texture dominated by alkali feldspar and quartz phenocrysts.
			NB-27 NB-28	Pumice fall: consistent in thickness well sorted, intercalate with ash falls.
		Qpl	NB-23 NB-24	Ignimbrite: well welded, associated with pumice flow, rich in crystal and rock fragments.
		Qpw	NB-26 NB-25 NB-30	Pumice flow: Poorly welded, interbedded with ash flow and ignimbrite and incorporate lapilli to boulder size lithics and pumice.
		Qrd	NB-14 NB-18 NB-17	Rhyolite lava flow: flow banded rhyolite, porphyritic in texture with alkali feldspar dominated phenocryst distribution.

Fig. 3

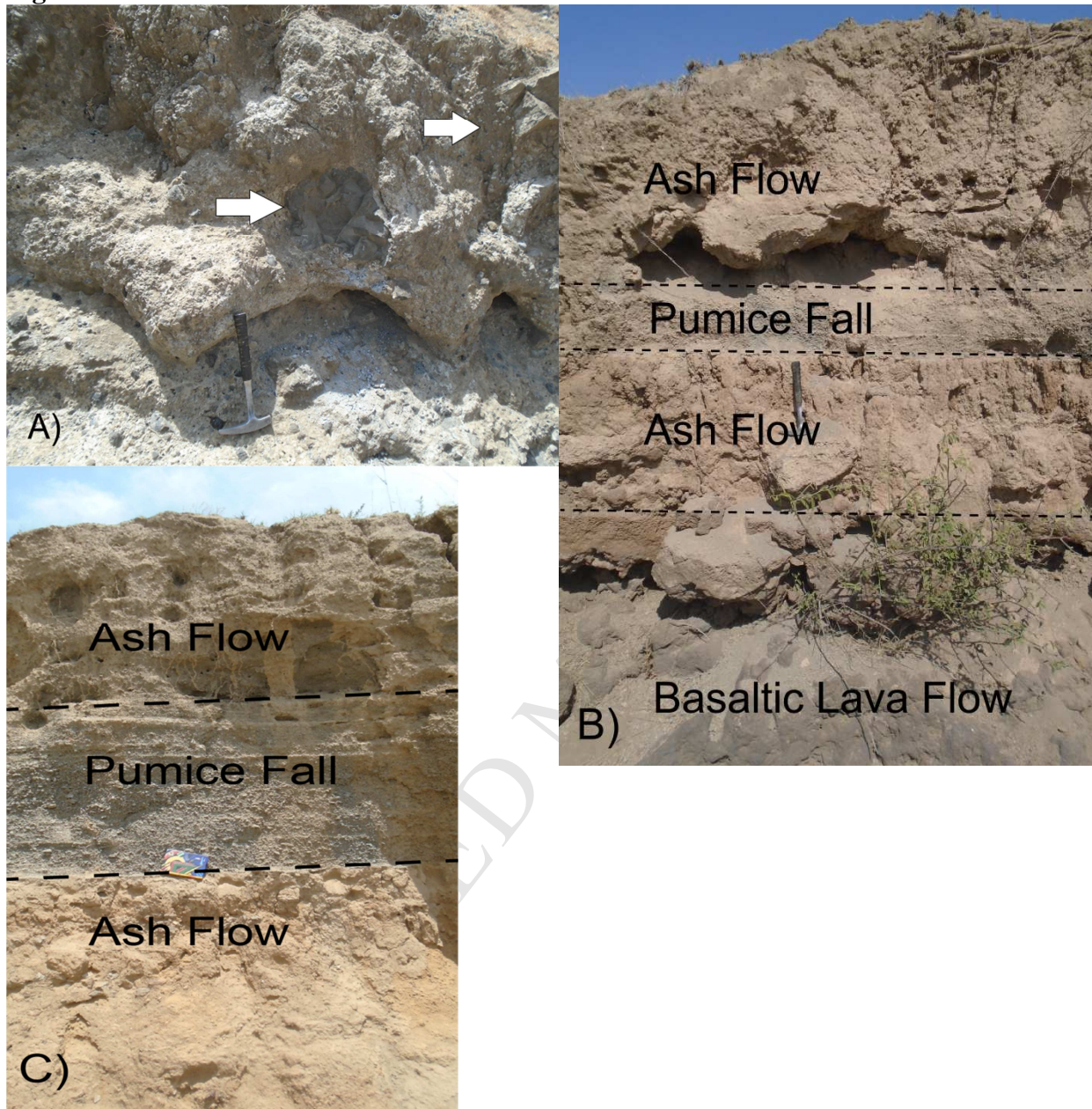


Fig. 4

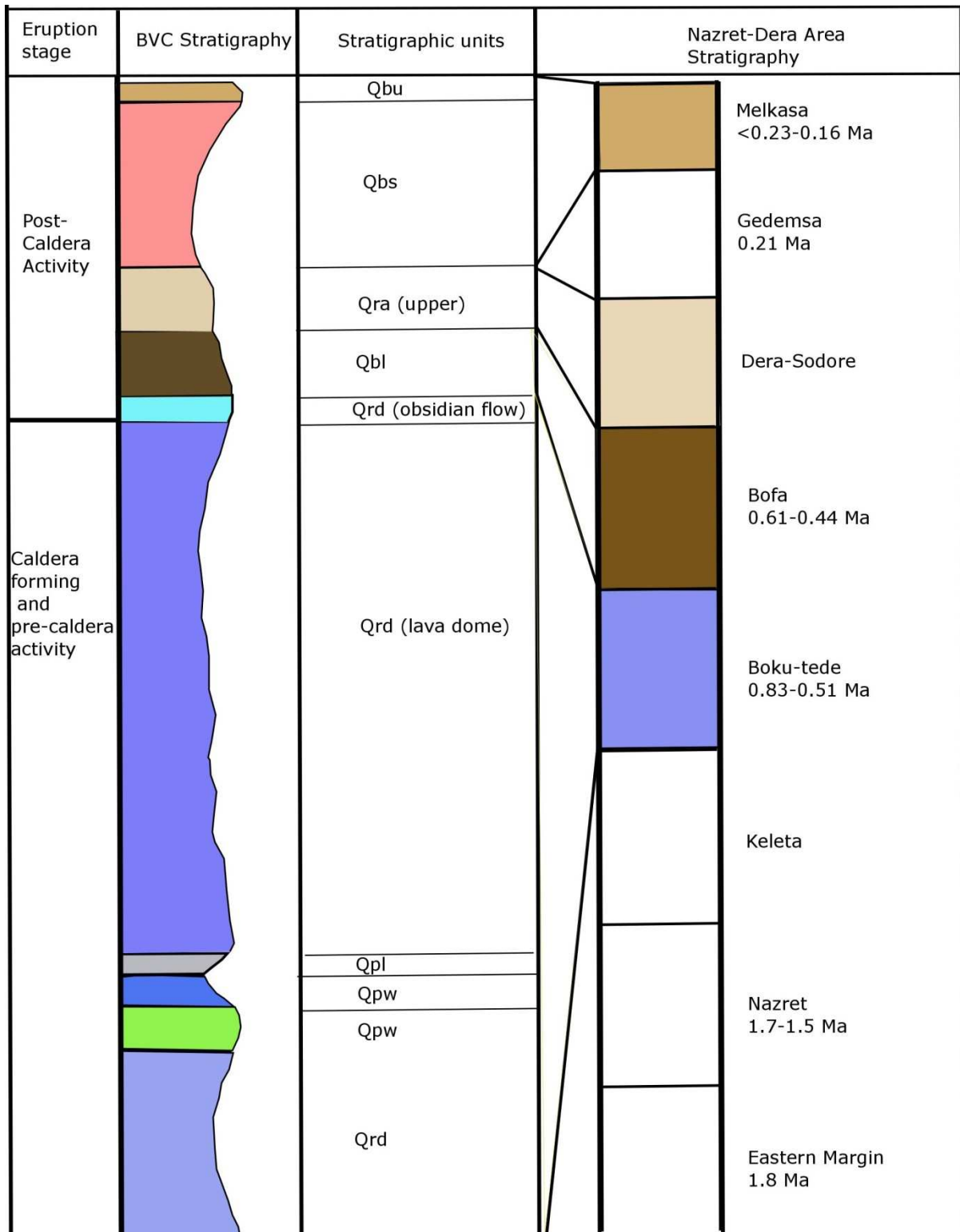


Fig. 5

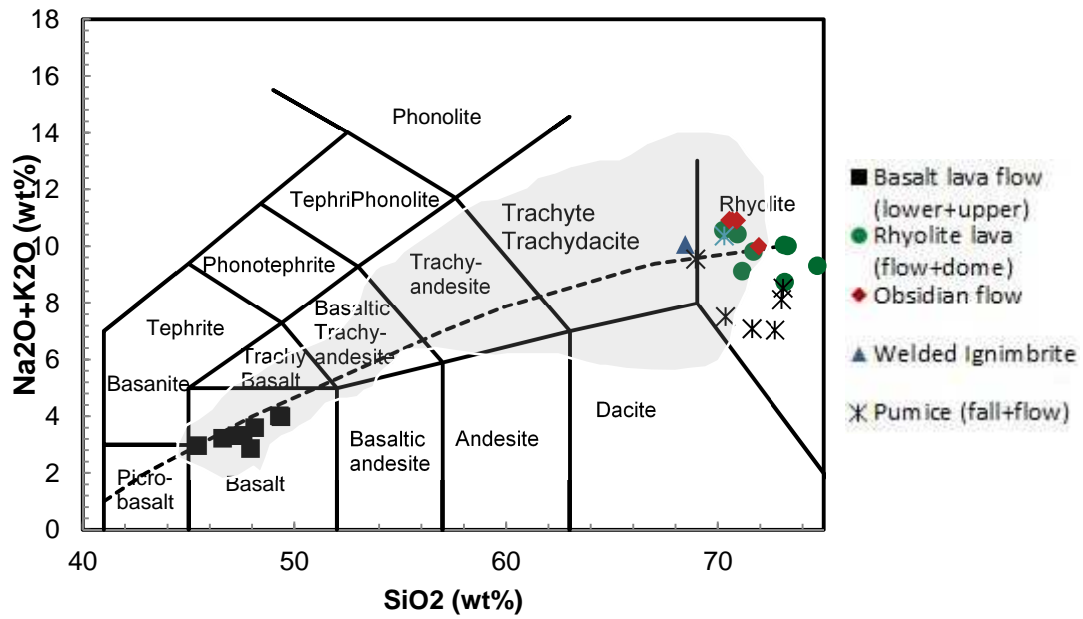


Fig.6

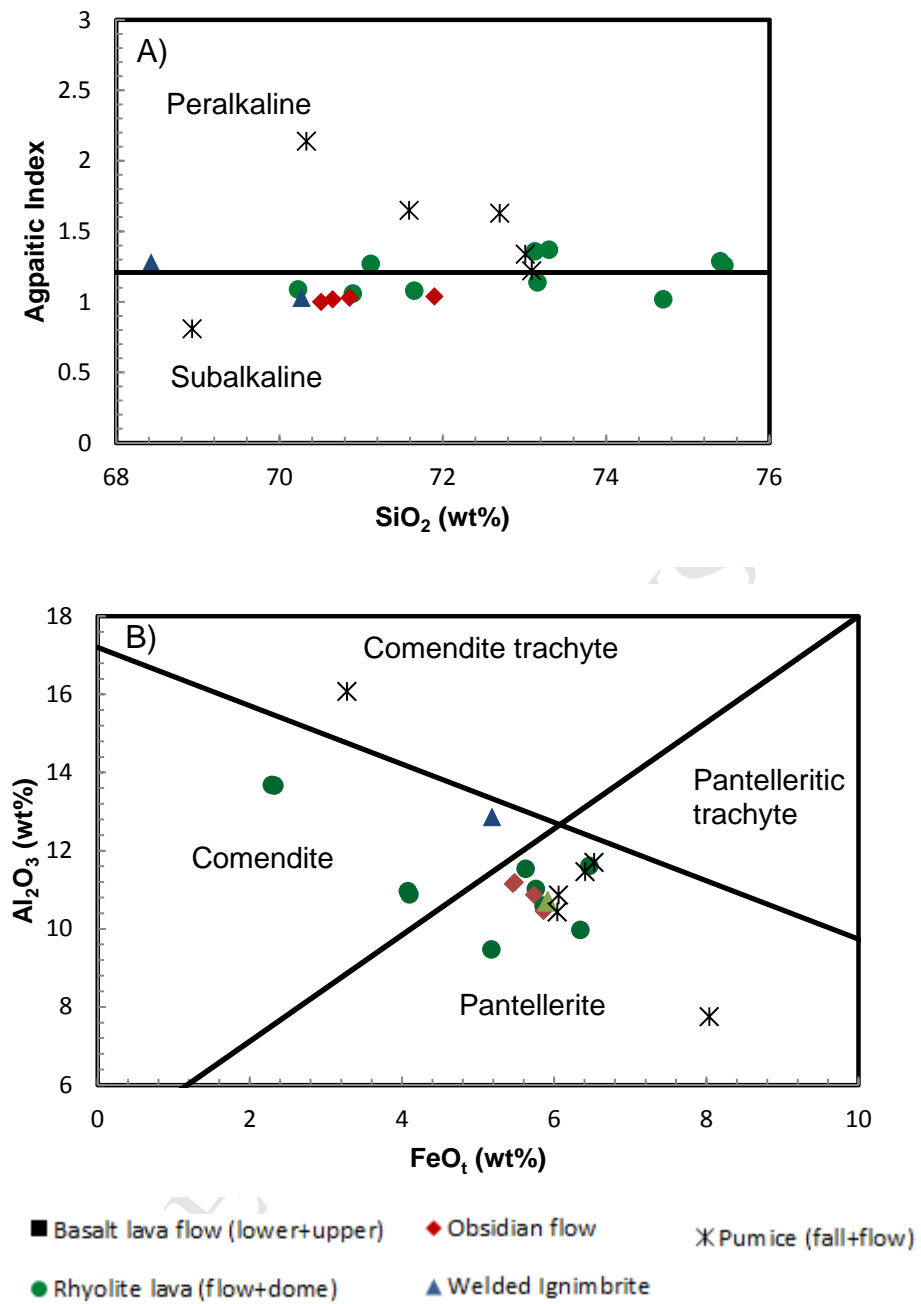


Fig.7

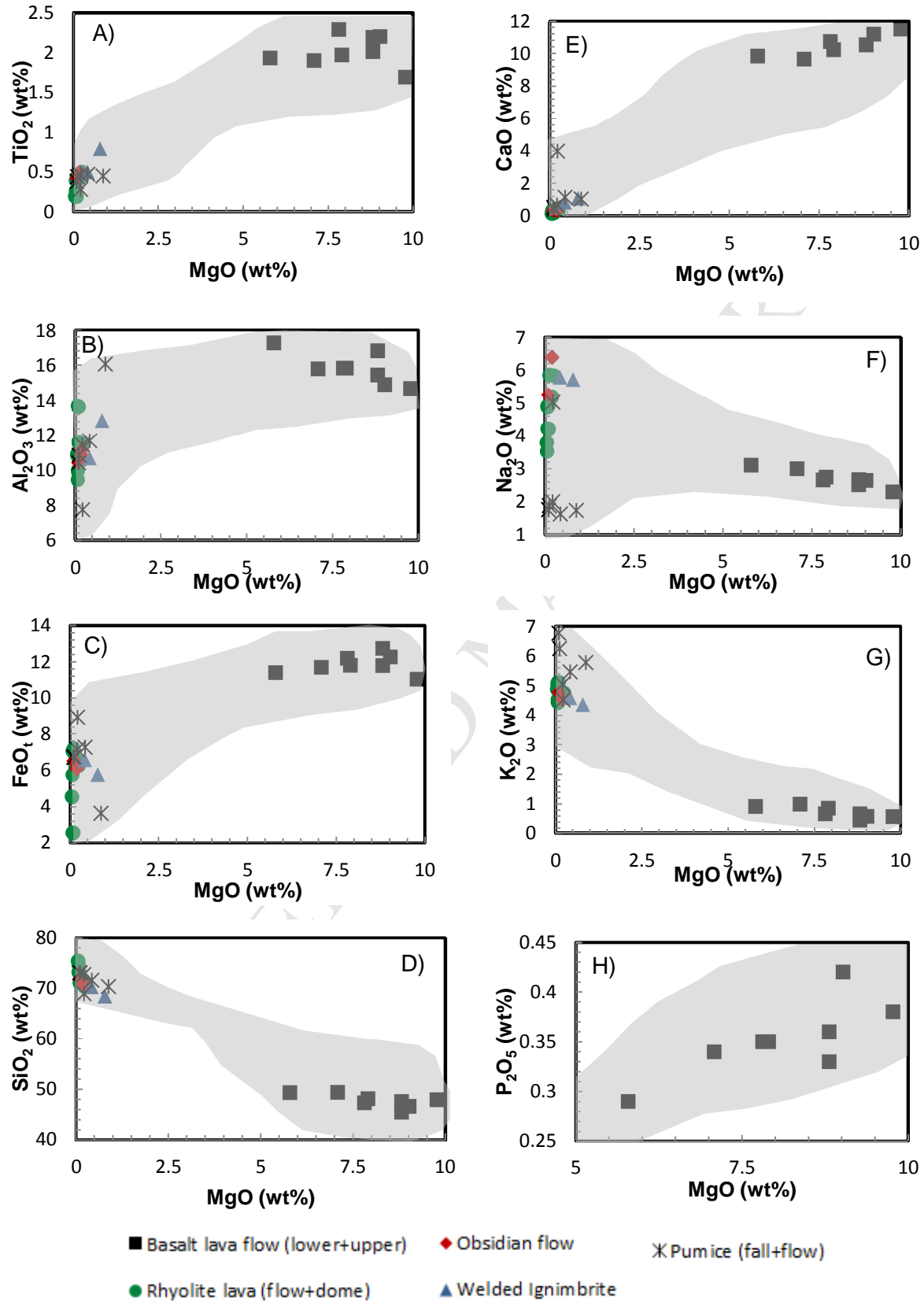




Fig. 8

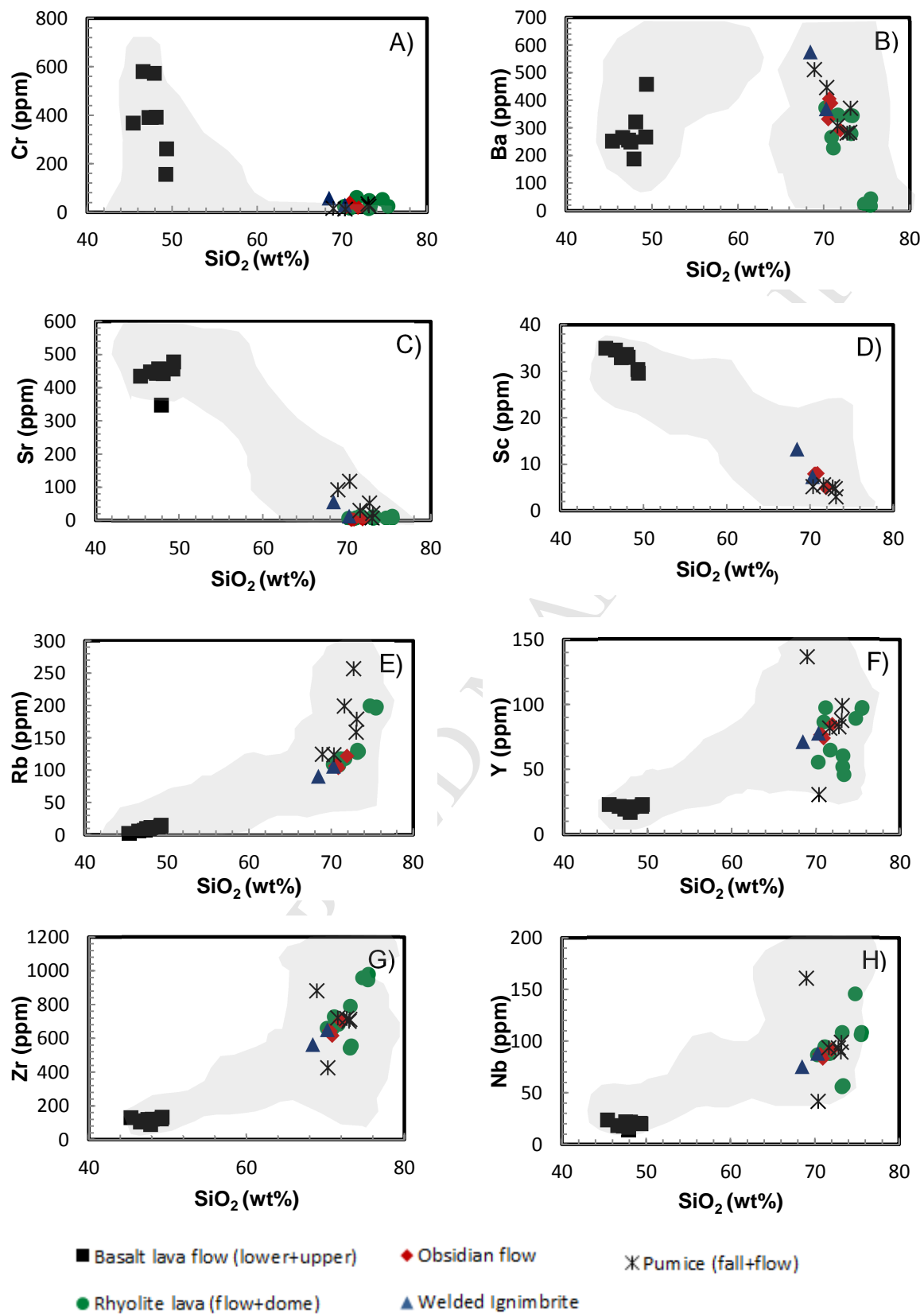




Fig. 9

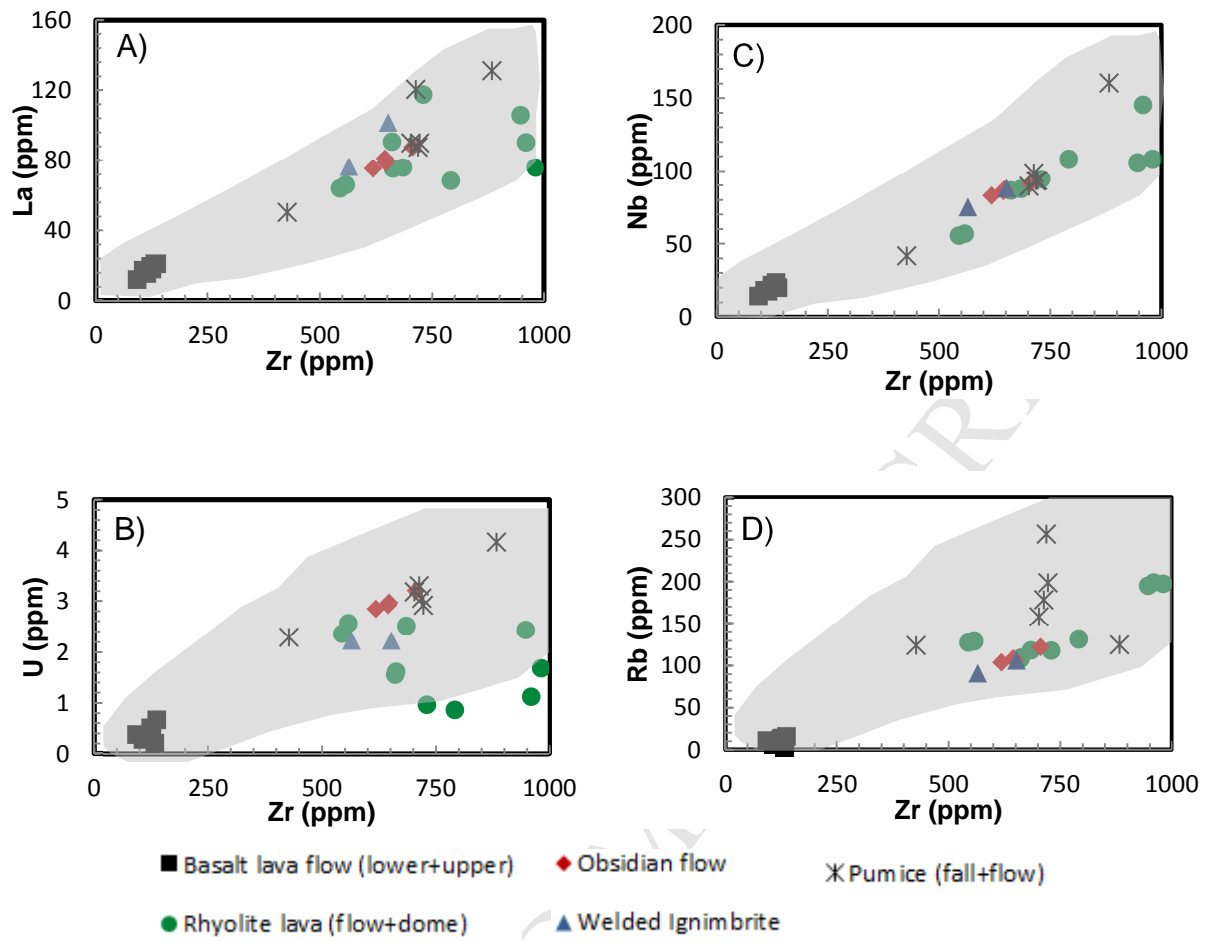


Fig. 10

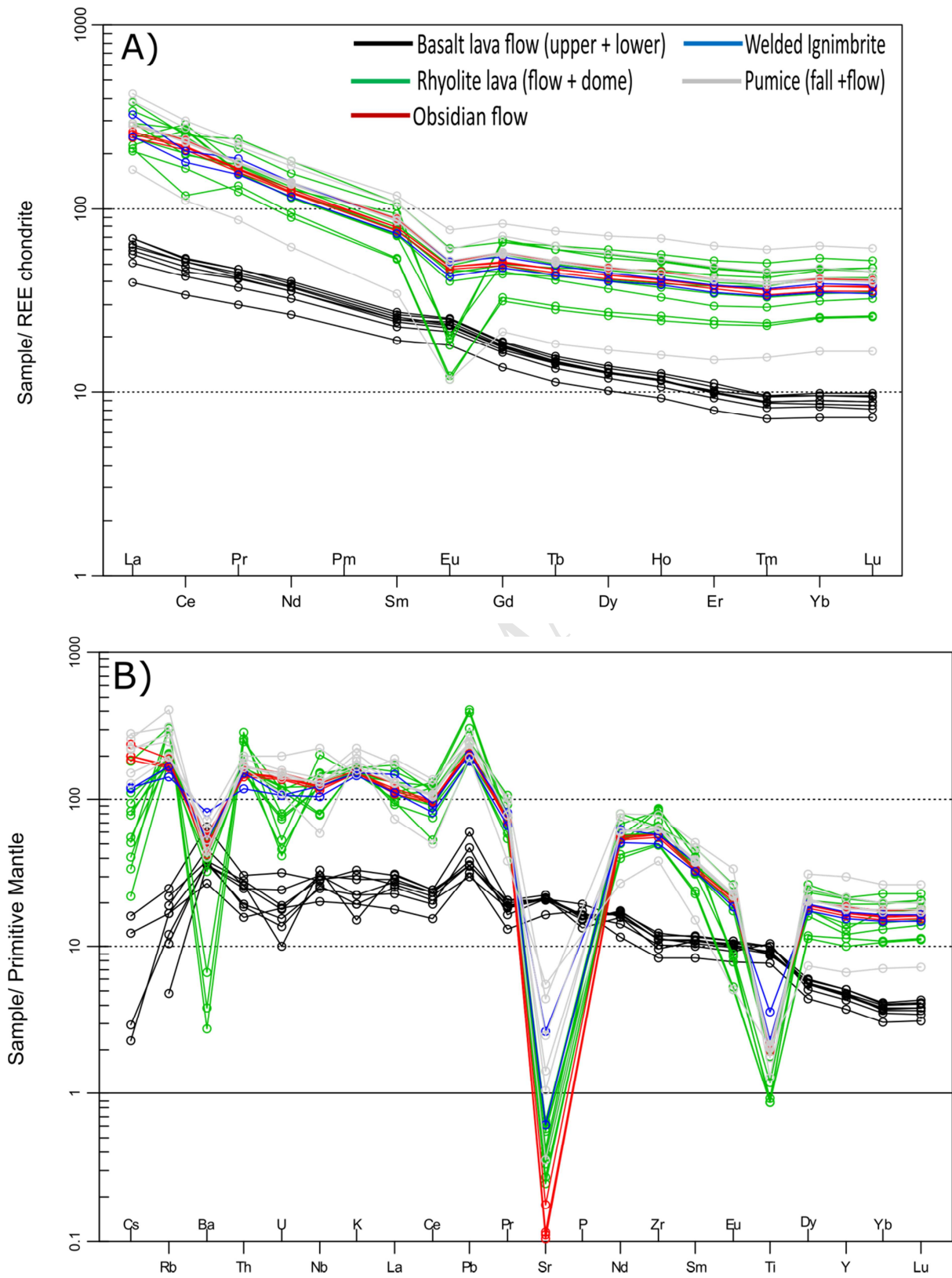
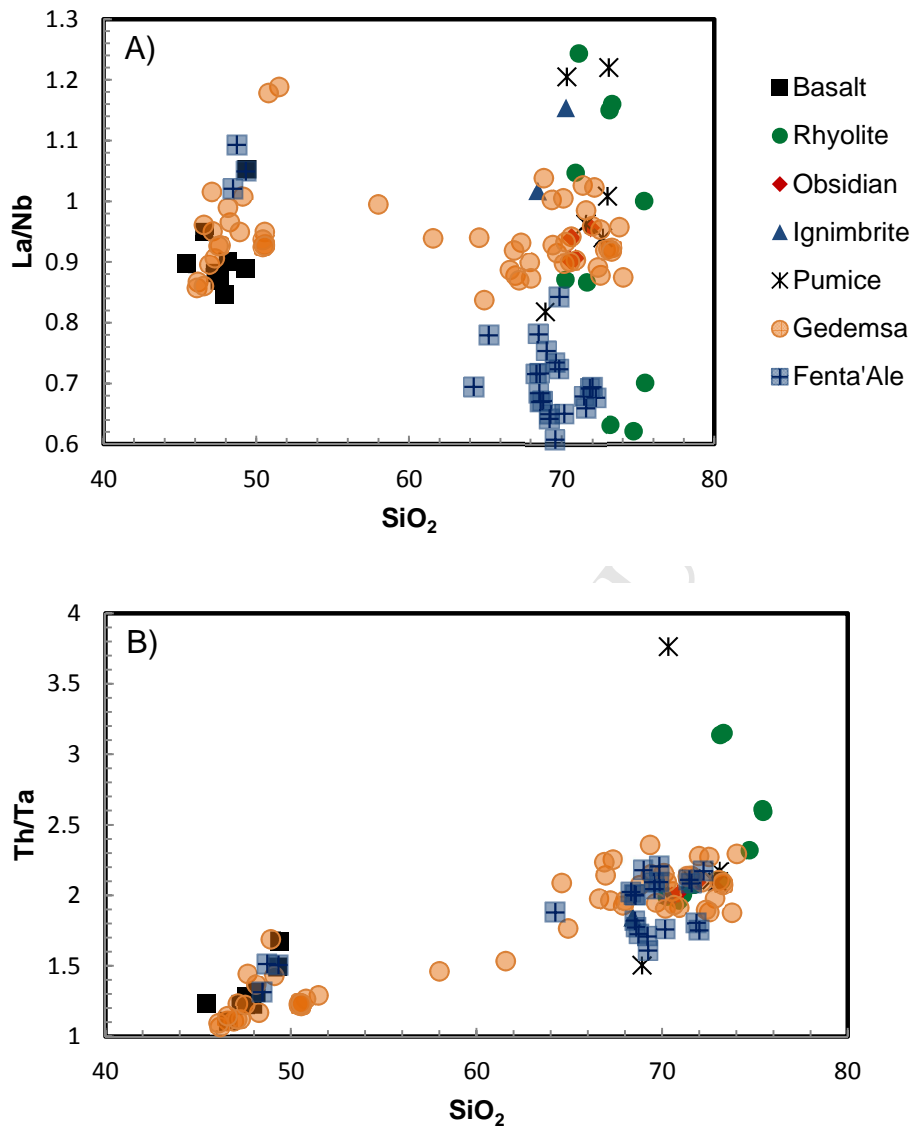


Fig. 11



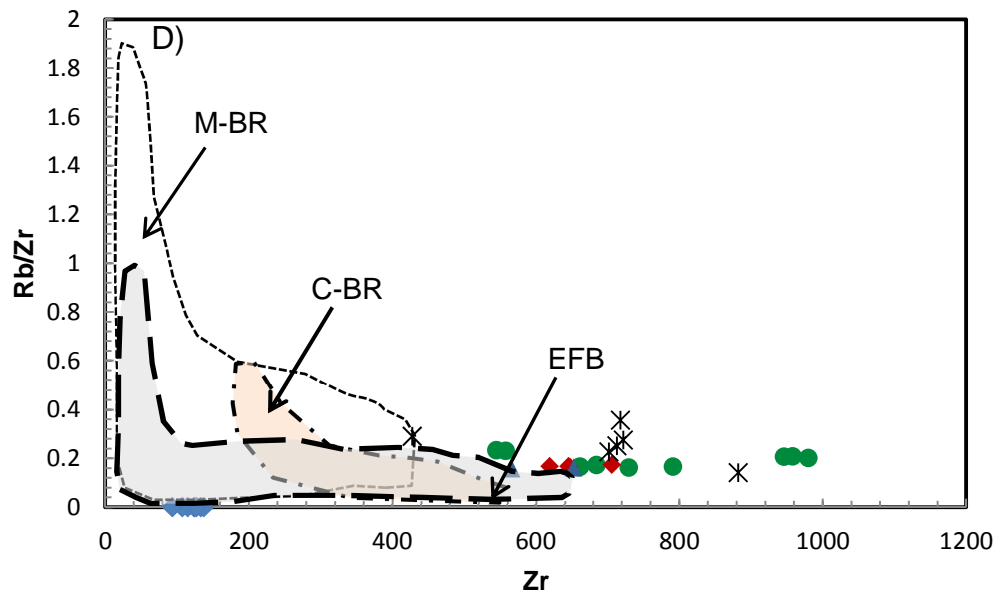
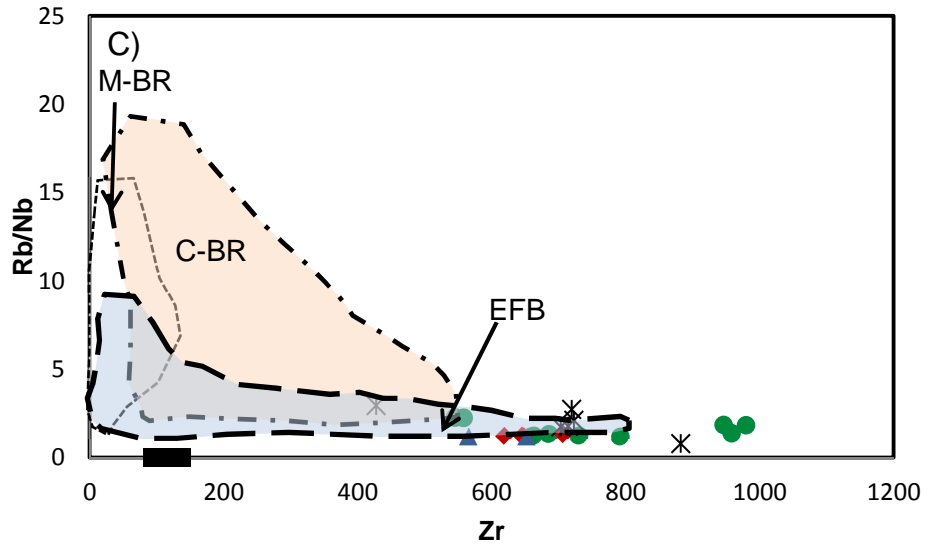
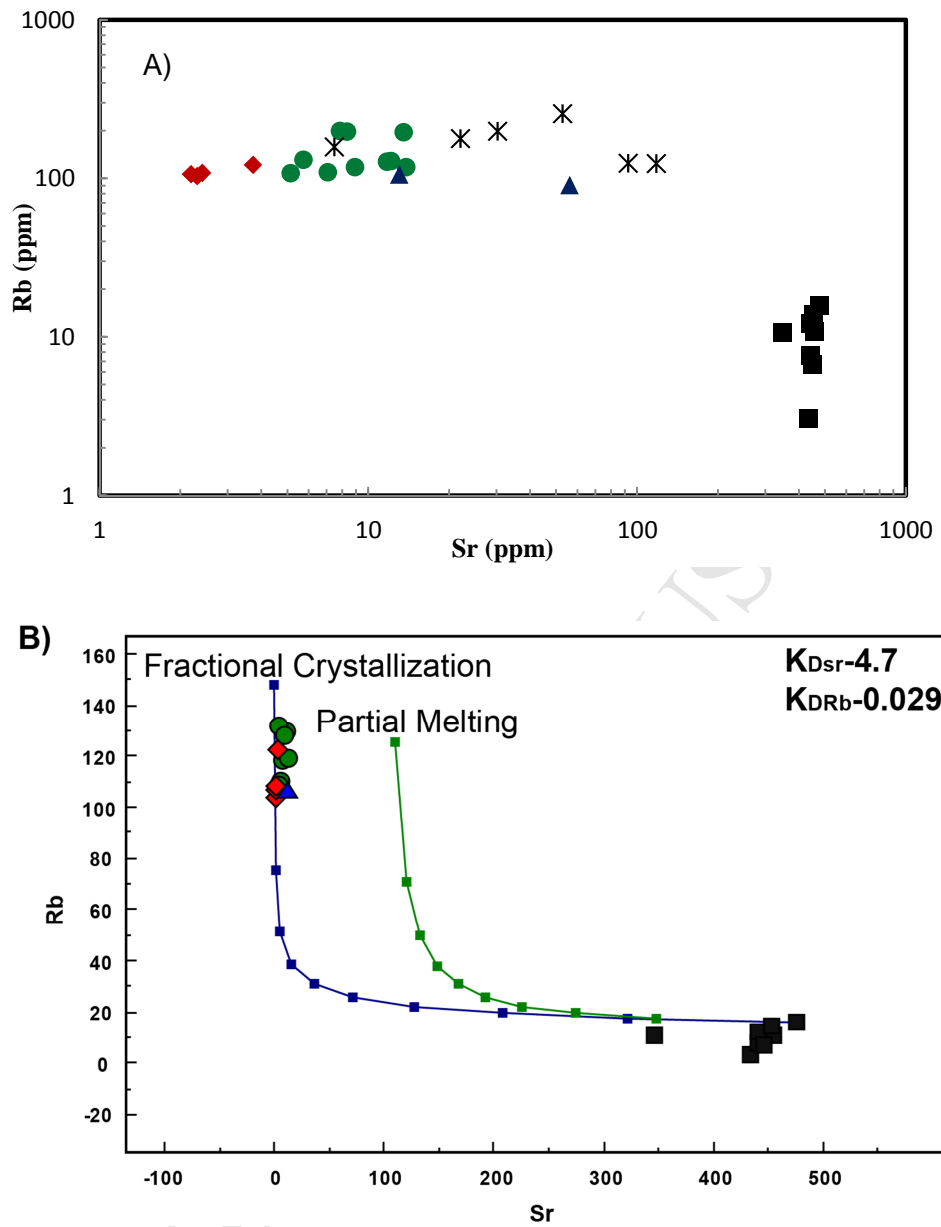


Fig. 12



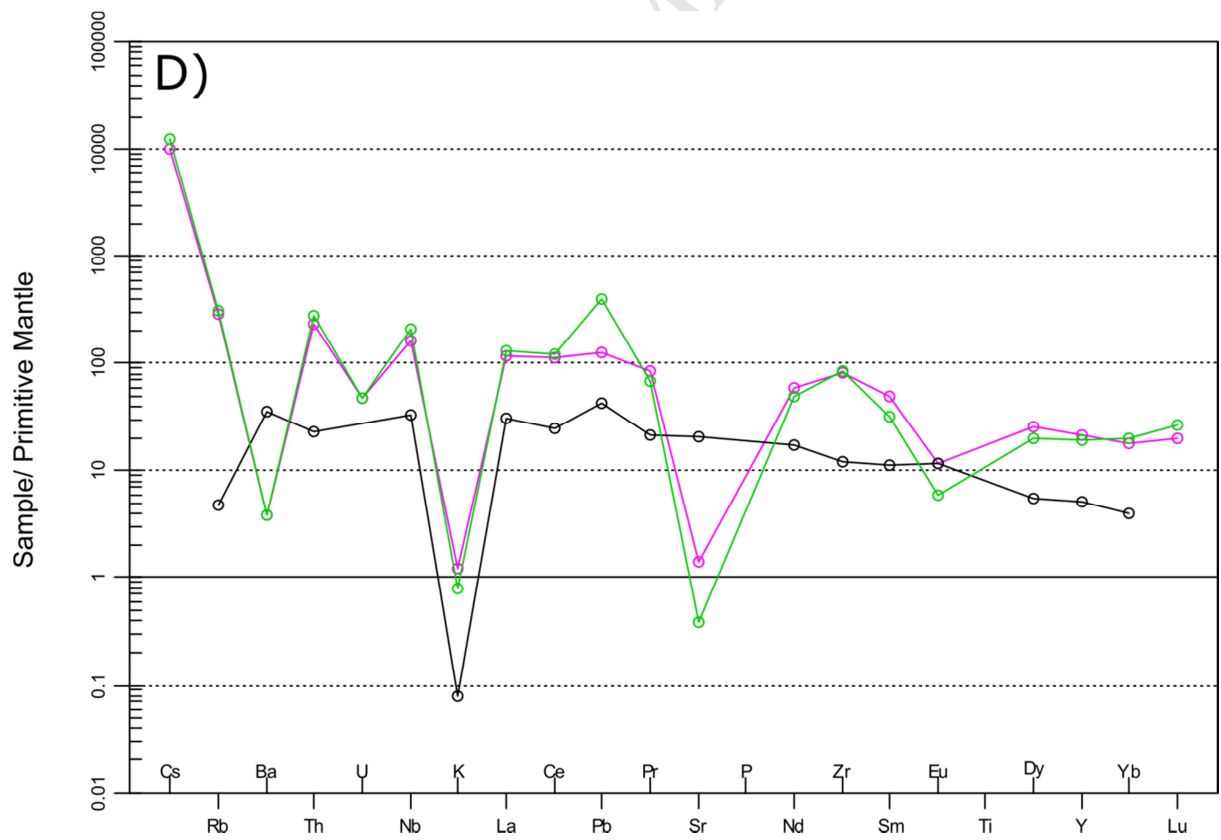
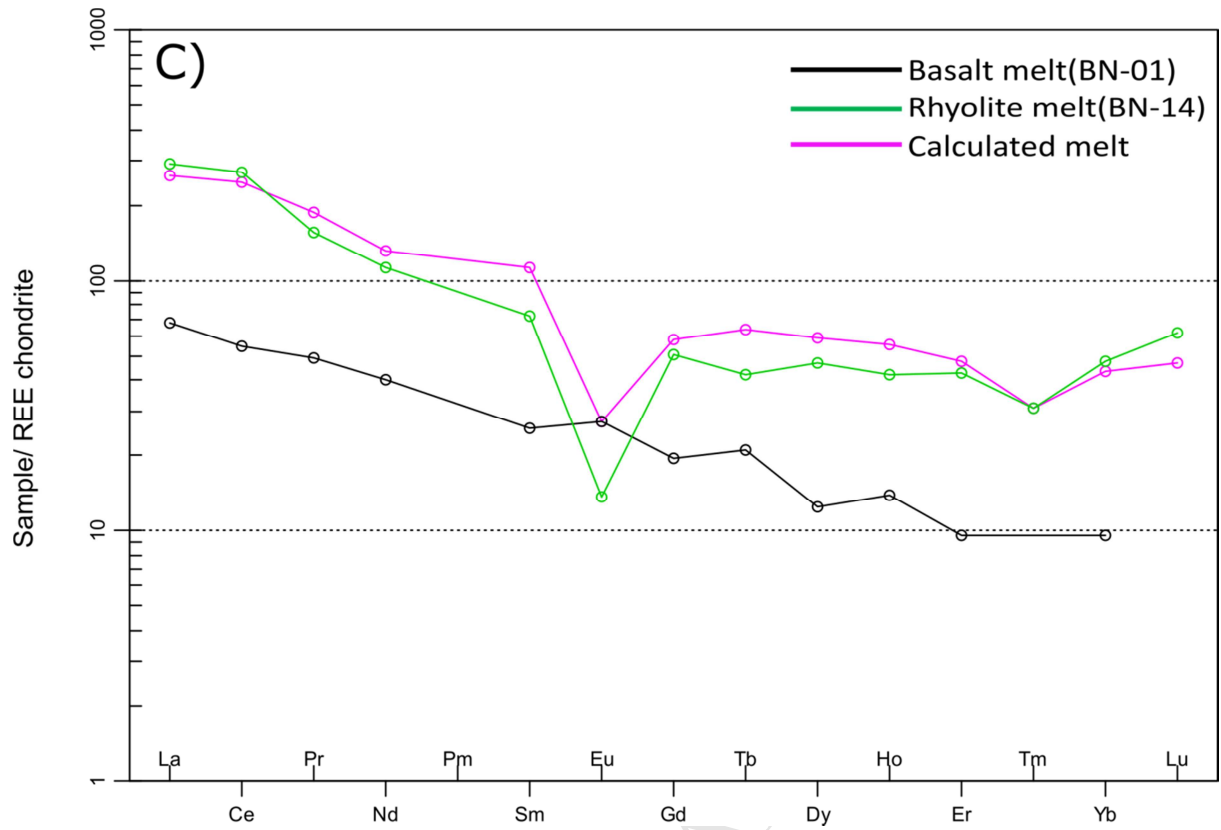
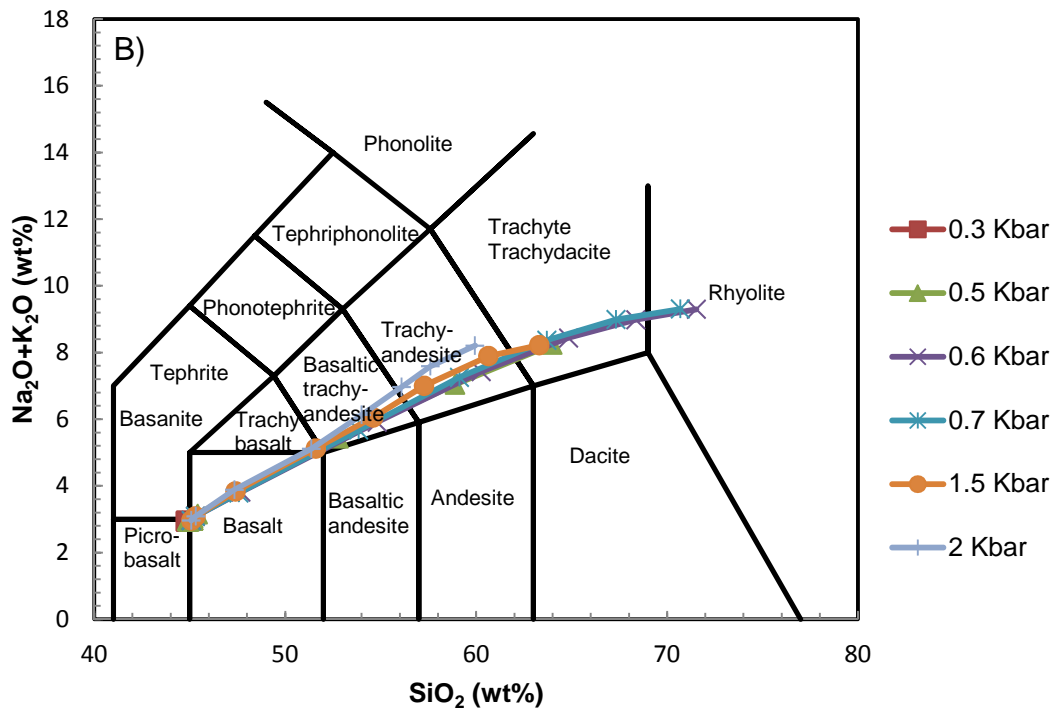
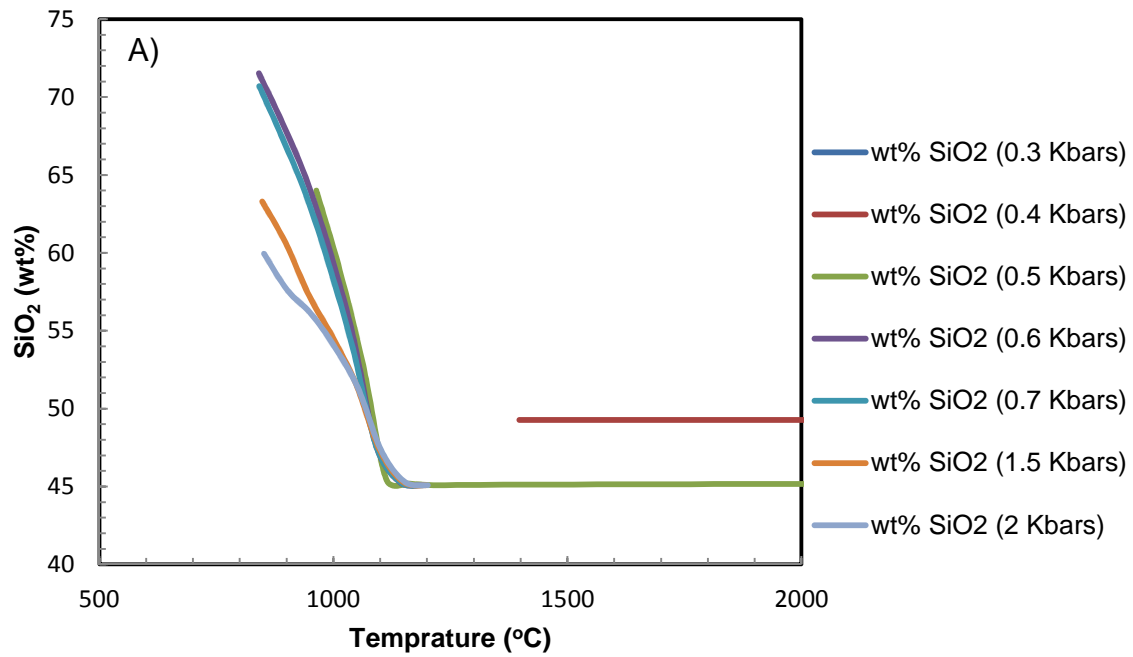
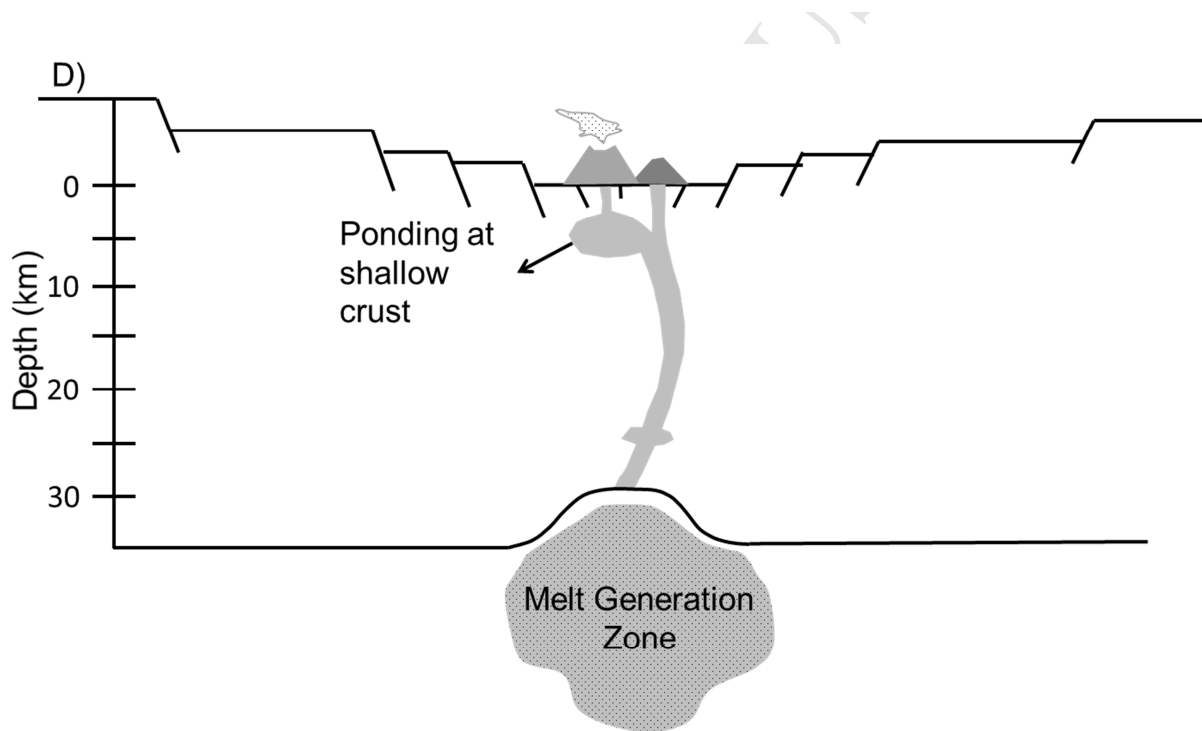
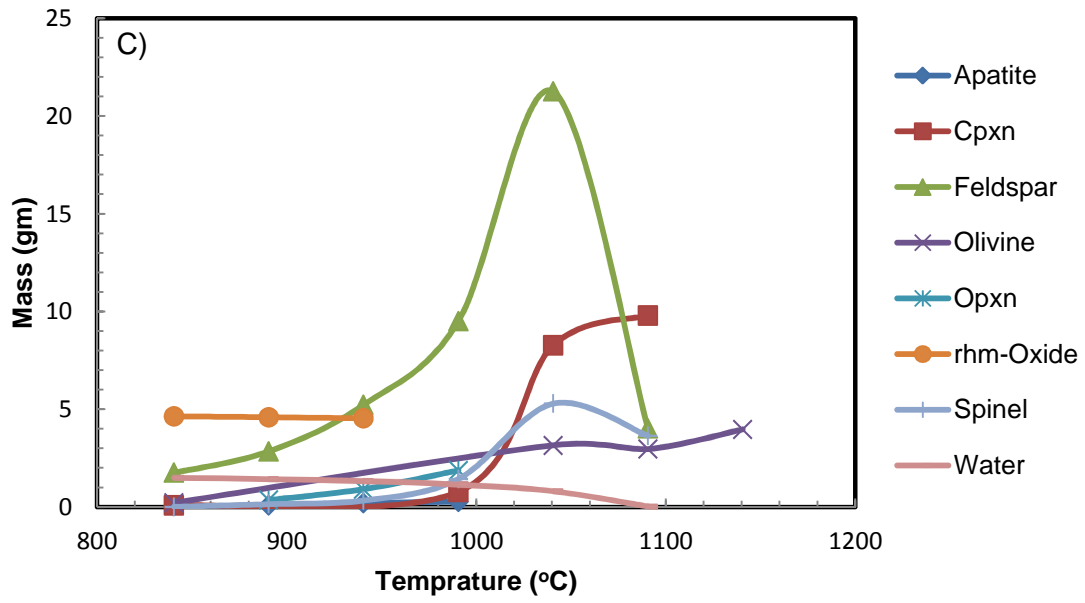


Fig. 13







**Highlight**

- ❖ Boku volcanic complex is a Quaternary silicic center found at the axial zone of Main Ethiopian Rift which is composed of volcanic products sourced from two main episodes of volcanic activity; Boku pre-caldera/caldera forming and post caldera eruptive activity.
- ❖ The chemical compositions are bimodal; mainly basaltic and silicic with a lack of intermediate composition. The basalts are transitional to weakly subalkaline and the silicic rocks are dominantly peralkaline rhyolite.
- ❖ The geochemistry result imply the two groups of the rock, basaltic and peralkaline rhyolite, has the same source and linked by a fractional crystallization process with minor crustal contamination